Article

Spike and nsp6 are key determinants of SARS-CoV-2 Omicron BA.1 attenuation

Da-Yuan Chen[1,2,15], Chue Vin Chin[1,2,15], Devin Kenney[2,3], Alexander H. Tavares[1,2], Nazimuddin Khan[1,2], Hasahn L. Conway[1,2], GuanQun Liu[4], Manish C. Choudhary[5,6], Hans P. Gertje[2], Aoife K. O'Connell[2], Scott Adams[2,3], Darrell N. Kotton[7,8], Alexandra Herrmann[9], Armin Ensser[9], John H. Connor[2,3], Markus Bosmann[8,10,11], Jonathan Z. Li[5,6], Michaela U. Gack[4], Susan C. Baker[12,13], Robert N. Kirchdoerfer[14], Yachana Kataria[10], Nicholas A. Crossland[2,10], Florian Douam[2,3] & Mohsan Saeed[1,2✉]

The SARS-CoV-2 Omicron variant is more immune evasive and less virulent than other major viral variants that have so far been recognized[1–12]. The Omicron spike (S) protein, which has an unusually large number of mutations, is considered to be the main driver of these phenotypes. Here we generated chimeric recombinant SARS-CoV-2 encoding the *S* gene of Omicron (BA.1 lineage) in the backbone of an ancestral SARS-CoV-2 isolate, and compared this virus with the naturally circulating Omicron variant. The Omicron S-bearing virus robustly escaped vaccine-induced humoral immunity, mainly owing to mutations in the receptor-binding motif; however, unlike naturally occurring Omicron, it efficiently replicated in cell lines and primary-like distal lung cells. Similarly, in K18-hACE2 mice, although virus bearing Omicron S caused less severe disease than the ancestral virus, its virulence was not attenuated to the level of Omicron. Further investigation showed that mutating non-structural protein 6 (nsp6) in addition to the S protein was sufficient to recapitulate the attenuated phenotype of Omicron. This indicates that although the vaccine escape of Omicron is driven by mutations in S, the pathogenicity of Omicron is determined by mutations both in and outside of the S protein.

As of December 2022, the successive waves of the COVID-19 pandemic have been driven by five major SARS-CoV-2 variants, known as variants of concern (VOC): Alpha (B.1.1.7), Beta (B.1.351), Gamma (P.1), Delta (B.1.617.2 and AY lineages) and Omicron (BA lineages)[13]. Omicron is the most recently recognized VOC, and was first documented in South Africa, Botswana and in a traveller from South Africa in Hong Kong in November 2021 (GISAID ID: EPI_ISL_7605742)[14,15]. It quickly swept through the world, displacing the previously dominant Delta variant within weeks and accounting for most new SARS-CoV-2 infections by January 2022 (refs. [16–18]). At least five lineages of Omicron have so far been identified: BA.1, BA.2, BA.3, BA.4 and BA.5. BA.1 (hereafter referred to as Omicron) exhibits a remarkable escape from infection- and vaccine-induced humoral immunity[3,19]. Furthermore, it is less virulent than other VOCs in humans and in vivo models of infection[4,5,7,11,12,20]. Omicron differs from the prototype SARS-CoV-2 isolate, Wuhan-Hu-1, by 59 amino acids; 37 of these changes are in the S protein, raising the possibility that S is at the heart of Omicron's pathogenic and antigenic behaviour.

S mutations affect Omicron replication in cell culture

The Omicron S protein contains 30 amino acid substitutions, 6 deletions and one insertion of 3 amino acids in length, as compared to Wuhan-Hu-1 (Extended Data Fig. 1). Twenty-five of these changes are unique to Omicron relative to other VOCs, although some of them have been reported in waste water and minor SARS-CoV-2 variants[21,22]. To test the role of the S protein in Omicron phenotype, we generated a chimeric recombinant virus containing the *S* gene of Omicron (USA-lh01/2021) and all other genes of an ancestral SARS-CoV-2 (GISAID EPI_ISL_2732373)[23] (Extended Data Fig. 2a). This chimeric virus, named Omi-S, was made by using a modified form of circular polymerase extension reaction (CPER)[24] (Extended Data Fig. 2b) that yielded highly concentrated virus stocks, containing 0.5×10^6–5×10^6 plaque-forming units (PFU) per ml, from transfected cells within two days of transfection (Extended Data Fig. 2c,d), obviating the need for further viral amplification.

[1]Department of Biochemistry, Boston University Chobanian and Avedisian School of Medicine, Boston, MA, USA. [2]National Emerging Infectious Diseases Laboratories, Boston University, Boston, MA, USA. [3]Department of Microbiology, Boston University Chobanian and Avedisian School of Medicine, Boston, MA, USA. [4]Florida Research and Innovation Center, Cleveland Clinic, Port St. Lucie, FL, USA. [5]Brigham and Women's Hospital, Boston, MA, USA. [6]Harvard Medical School, Cambridge, MA, USA. [7]Center for Regenerative Medicine of Boston University and Boston Medical Center, Boston, MA, USA. [8]The Pulmonary Center and Department of Medicine, Boston University Chobanian and Avedisian School of Medicine, Boston, MA, USA. [9]Institute of Clinical and Molecular Virology, University Hospital Erlangen, Friedrich-Alexander Universität Erlangen-Nürnberg, Erlangen, Germany. [10]Department of Pathology and Laboratory Medicine, Boston University Chobanian and Avedisian School of Medicine, Boston, MA, USA. [11]Center for Thrombosis and Hemostasis, University Medical Center of the Johannes Gutenberg University, Mainz, Germany. [12]Department of Microbiology and Immunology, Stritch School of Medicine, Loyola University Chicago, Maywood, IL, USA. [13]Infectious Disease and Immunology Research Institute, Stritch School of Medicine, Loyola University Chicago, Maywood, IL, USA. [14]Department of Biochemistry, College of Agricultural and Life Sciences, University of Wisconsin-Madison, Madison, WI, USA. [15]These authors contributed equally: Da-Yuan Chen, Chue Vin Chin. ✉e-mail: msaeed1@bu.edu
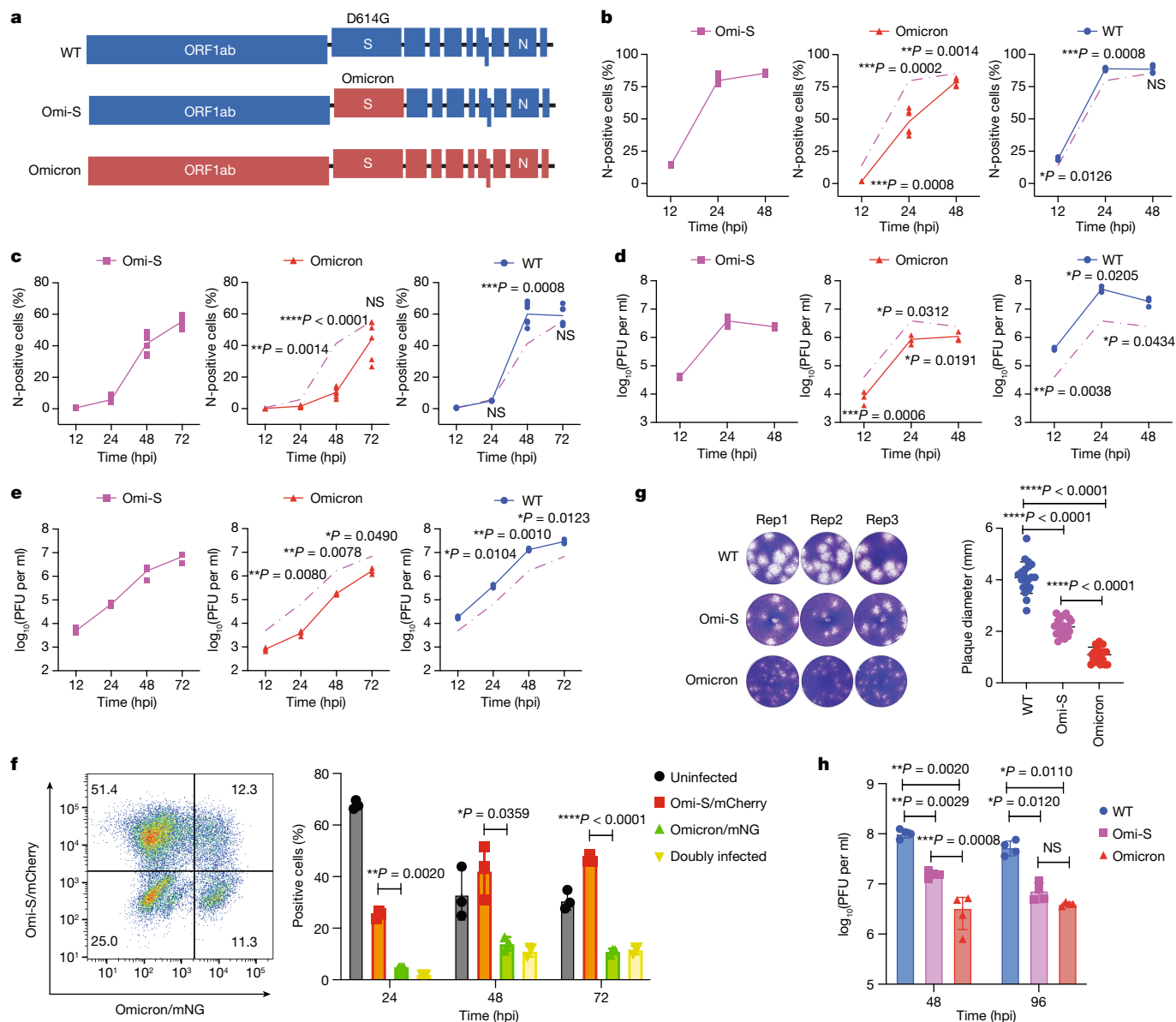
Fig. 1 | Effect of S on the in vitro growth kinetics of Omicron. a, Schematic of viruses. S, spike; N, nucleocapsid. **b–e**, ACE2/TMPRSS2/Caco-2 cells (**b,d**) and Vero E6 cells (**c,e**) were infected at an MOI of 0.01, and the percentage of N-positive cells (*n* = 6 replicates) (**b,c**) and the release of infectious particles (*n* = 3 replicates) (**d,e**) were determined by flow cytometry and by plaque assay, respectively. **f**, ACE2/TMPRSS2/Caco-2 cells were infected with virus mixtures at a 1:1 ratio to obtain the final MOI of 0.005 for each virus. The cells were fixed at the indicated times and subjected to flow cytometry. Left, representative dot plot; right, percentage of uninfected, Omi-S/mCherry-infected, Omicron/mNeoGreen (Omicron/mNG)-infected and doubly infected cells. Singly infected cells were used for compensation. Error bars, mean ± s.d. (*n* = 3 replicates).

g, Plaque sizes. Left, representative images of plaques on ACE2/TMPRSS2/Caco-2 cells. Right, the diameter of plaques is plotted as the mean ± s.d. of 20 plaques per virus. **h**, Human iAT2 epithelial cells were infected at an MOI of 2.5 for 48 h or 96 h. The apical side of cells was washed with 1× phosphate-buffered saline (PBS) and the levels of infectious virus particle were measured by plaque assay. Error bars, mean ± s.d. (*n* = 4 replicates). Experiments were repeated twice, with each experimental repeat containing 3 (**b–g**) or 4 (**h**) replicates. *P* values were calculated by a two-tailed, unpaired *t*-test with Welch's correction. **P* < 0.05, ***P* < 0.01, ****P* < 0.001 and *****P* < 0.0001; NS, not significant. The gating strategy for flow cytometry is shown in Supplementary Fig. 1.

We first compared the infection efficiency of Omi-S with an ancestral D614G-containing virus (GISAID EPI_ISL_2732373; generated by CPER; hereafter referred to as wild type (WT)) and an Omicron isolate (USA-lh01/2021) in cell culture (Fig. 1a). For this, we infected ACE2- and TMPRSS2-expressing Caco-2 (hereafter, ACE2/TMPRSS2/Caco-2) and Vero E6 cells with Omi-S, WT and Omicron at a multiplicity of infection (MOI) of 0.01, and monitored viral propagation by flow cytometry and plaque formation assay. The WT virus and Omi-S spread rapidly in ACE2/TMPRSS2/Caco-2 cells, yielding 89% and 80% infected cells, respectively, at 24 hours post-infection (hpi) (Fig. 1b). By contrast, Omicron replicated more slowly, leading to 48% infected cells at 24 hpi.

A similar pattern was seen in Vero E6 cells, in which 60% and 41% of cells were positive for WT and Omi-S, respectively, at 48 hpi, as opposed to 10% for Omicron (Fig. 1c). The plaque assay showed that although both Omi-S and Omicron produced lower levels of infectious virus particles compared with WT, the viral titre of Omi-S was significantly higher than that of Omicron. In ACE2/TMPRSS2/Caco-2 cells, Omi-S produced 5.1-fold (*P* = 0.0006) and 5.5-fold (*P* = 0.0312) more infectious particles than Omicron at 12 hpi and 24 hpi, respectively (Fig. 1d). Similarly, in Vero E6 cells, the infectious virus titres of Omi-S were 17-fold (*P* = 0.0080) and 11-fold (*P* = 0.0078) higher than that of Omicron at 24 hpi and 48 hpi, respectively (Fig. 1e). The difference between viruses

became less obvious at later time points owing to higher cytotoxicity caused by Omi-S compared to Omicron (Extended Data Fig. 3a).

The increased replication efficiency of Omi-S relative to Omicron was preserved when tested at varying MOIs (Extended Data Fig. 3b). We further confirmed the fitness advantage of Omi-S over Omicron by a direct competition assay. For this, we first generated recombinant Omicron (rOmicron), which, in our cell culture assays, mimicked the replication kinetics of natural Omicron (Extended Data Fig. 4). Next, we created mCherry-containing Omi-S and mNeonGreen-containing Omicron, and inoculated ACE2/TMPRSS2/Caco-2 cells with these viruses mixed at a 1:1 ratio. Flow cytometric analysis of infected cells at various times of infection showed that Omi-S/mCherry was clearly superior to Omicron/mNeonGreen in terms of replication (Fig. 1f). Finally, the higher infection efficiency of Omi-S was also reflected in the plaque size; although WT virus produced the largest plaques (around 4.1 mm), the size of Omi-S plaques (around 2.2 mm) was twofold ($P < 0.0001$) larger than that of Omicron plaques (around 1.1 mm) (Fig. 1g). These results indicate that although mutations in the S protein influence the infection efficiency of Omicron, they do not fully explain the Omicron phenotype.

Several lines of evidence indicated that the S protein incorporated into Omi-S behaved the same way as in natural Omicron. For instance, as described previously[20,25], Omicron S was poorly cleaved compared to WT S; whereas 71% of S in WT virions was in the cleaved form, only 45% and 47% was cleaved in Omi-S and Omicron, respectively (Extended Data Fig. 5a). The same pattern of S cleavage was evident in virus-infected cells (WT, 63% cleaved; Omi-S, 33% cleaved; Omicron, 42% cleaved) (Extended Data Fig. 5b). These experiments also revealed that Omicron S was inefficiently incorporated into virus particles compared to WT S (S to nucleocapsid (N) ratio: 3.40 for WT virus, 1.91 for Omi-S and 2.04 for Omicron) (Extended Data Fig. 5a). Similarly, both Omi-S and Omicron produced smaller syncytia compared to the WT virus, an observation that has previously been reported for Omicron[20,26] (Extended Data Fig. 5c). Finally, consistent with the published literature[25], Omi-S and Omicron showed a preference for cathepsin-mediated entry, as reflected by their higher sensitivity to the cathepsin inhibitor E64d (Extended Data Fig. 6).

We next compared the replication kinetics of WT, Omi-S and Omicron in lung epithelial cells, which form a major viral replication site in patients with COVID-19 (refs. [27,28]). Accordingly, we used human induced pluripotent stem (iPS)-cell-derived lung alveolar type 2 epithelial (iAT2) cells. AT2 cells represent an essential cell population in the distal lung and constitute one of the primary targets of SARS-CoV-2 infection[28,29]. We infected iAT2 cells, grown as an air–liquid interface (ALI) culture, at an MOI of 2.5 and monitored the secretion of viral progeny on the apical side of cells at 48 hpi and 96 hpi. In congruence with the results obtained from cell lines, WT virus produced the highest levels of infectious virus particles (Fig. 1h). Among Omi-S and Omicron, the former yielded around fivefold ($P = 0.0008$) higher infectious viral titre at 48 hpi. The viral titres for WT and Omi-S decreased at 96 hpi compared to 48 hpi owing to the cytopathic effect (CPE) of infection. However, no CPE was seen for Omicron, leading to sustained production of infectious virions. Overall, these results corroborate the conclusion that mutations in S do not fully account for the attenuated replication capacity of Omicron in cell culture.

Minimal role of S in Omicron pathogenicity in mice

To examine whether Omi-S exhibits higher in vivo fitness compared with Omicron, we investigated the infection outcome of Omi-S relative to WT SARS-CoV-2 and Omicron in K18-hACE2 mice. In agreement with the published literature[4,5], intranasal inoculation of mice (aged 12–20 weeks) with Omicron (10^4 PFU per mouse) caused no significant weight loss, whereas inoculation with WT virus triggered a rapid decrease in body weight, with all mice losing over 20% of their initial body weight

by 8 days post-infection (dpi) (Fig. 2a). Notably, 80% of mice infected with Omi-S also lost over 20% of their body weight by 9 dpi (Fig. 2a and Extended Data Fig. 7a). The evaluation of clinical scores (a cumulative measure of weight loss, abnormal respiration, aberrant appearance, reduced responsiveness and altered behaviour) also revealed a similar pattern; whereas Omicron-infected mice exhibited few to no signs of clinical illness, the health of those infected with WT and Omi-S rapidly deteriorated, with the WT virus causing a more severe disease ($P = 0.0102$) (Fig. 2b and Extended Data Fig. 7b). Because SARS-CoV-2 causes fatal infection in K18-hACE2 mice[4], we compared the survival of mice after viral infection. Agreeing with the results of body-weight loss and clinical score, WT and Omi-S caused mortality rates of 100% (6/6) and 80% (8/10), respectively. By contrast, all mice infected with Omicron survived (Fig. 2c). These findings, which are consistent with a recent publication[30], indicate that the S protein is not the exclusive determinant of Omicron's pathogenicity in K18-hACE2 mice.

Next, we compared the propagation of Omi-S with Omicron and WT SARS-CoV-2 in the lungs and nasal turbinates of K18-hACE2 mice. The mice (12–20 weeks old) were intranasally challenged with 10^4 PFU (seven mice per virus), and viral titres in mice lungs were measured at 2 and 4 dpi. Consistent with in vitro findings, the infectious virus titre in the lungs of WT-infected mice was higher than that detected in mice infected with the other two viruses (Fig. 2d). Notably, however, Omi-S-infected mice produced 30-fold ($P = 0.0286$) more infectious virus particles compared with Omicron-infected mice at 2 dpi. The titre decreased at 4 dpi for WT- and Omi-S-infected mice, but it showed an increasing trend for Omicron-infected mice, pointing to the possibility of mild but persistent infection by Omicron in K18-hACE2 mice. All three variants recovered from the lungs of mice maintained the same plaque size phenotype as the original inoculum, indicating that replication in mice had no detectable effect on genotypes of these viruses (data not shown).

To evaluate the viral pathogenicity in lungs and nasal turbinates of K18-hACE2 mice, we performed histopathological analysis of these tissues at 2 dpi. As previously reported[4,31], an extensive near-diffused immunoreactivity of the SARS-CoV-2 N protein was detected in lung alveoli of mice infected with WT virus (Fig. 2e). By contrast, Omi-S and Omicron infection produced localized foci of alveolar staining with fewer foci for Omicron compared with Omi-S. The most marked phenotype was seen in bronchiolar epithelium, in which Omi-S caused pronounced, routinely circumferential infection, with around 10–15% of bronchioles being positive for viral N protein at 2 dpi, whereas only 3–5% of bronchioles were N-positive for Omicron (Fig. 2f). WT virus infected around 1% of bronchioles and in all cases only included a single isolated epithelial cell per bronchiole. Furthermore, bronchiolar infection was associated with epithelial necrosis in Omi-S-infected mice, as determined through serial haematoxylin and eosin (H&E) section analysis, whereas no histological evidence of airway injury was observed in Omicron- or WT-infected mice (Extended Data Fig. 8a,b). The nasal turbinates of mice inoculated with WT and Omi-S viruses both contained abundant SARS-CoV-2-positive cells, which were associated with overt cytopathic effects, whereas Omicron produced rare, sporadic positive cells, with no apparent signs of epithelial injury (Extended Data Fig. 8c). Overall, these findings suggest that replication of Omicron in the mice respiratory tract is substantially attenuated compared to Omi-S, supporting our conclusion that mutations in S are only partially responsible for the attenuated pathogenicity of Omicron.

Mutations in S and nsp6 define Omicron attenuation

In addition to the S protein, Omicron has amino acid changes in non-structural protein 3 (nsp3), nsp4, nsp5, nsp6, nsp14, envelope (E), membrane (M) and N proteins, when compared with WT virus (Extended Data Fig. 9a). To identify non-spike proteins that are involved in Omicron attenuation, we generated a large panel of fluorescently labelled
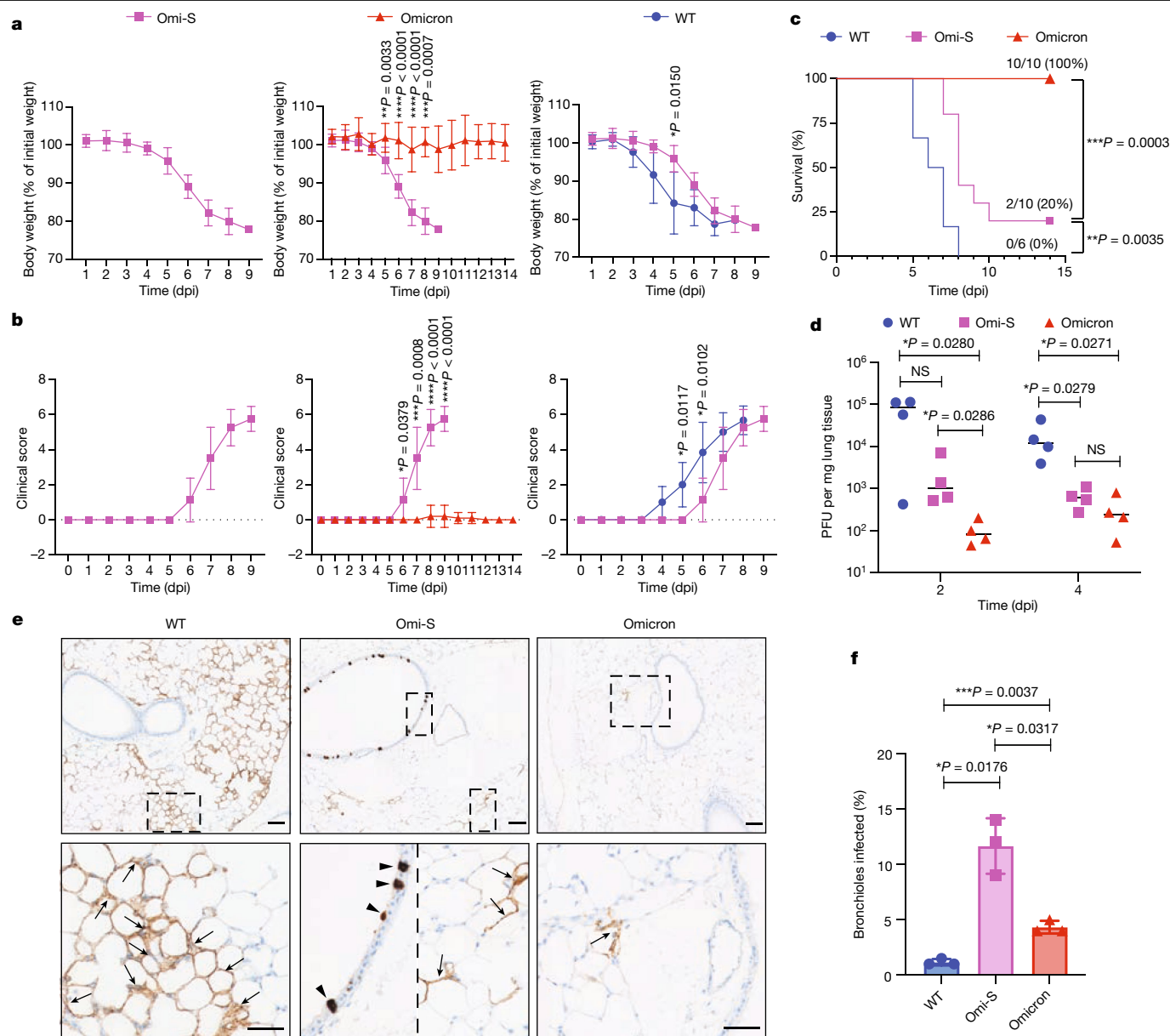
Fig. 2 | Role of S in Omicron pathogenicity. a–c, Male and female K18-hACE2 mice (aged 12–20 weeks) were intranasally inoculated with 1×10^4 PFU of WT ($n = 6$ mice), Omi-S ($n = 10$ mice) or Omicron ($n = 10$ mice) virus. Two independently generated virus stocks were used in this experiment. Body weight (**a**), clinical score (**b**) and survival (**c**) were monitored daily for 14 days. Mice that lost 20% of their initial body weight were euthanized. **d,e**, K18-hACE2 mice were intranasally inoculated with 1×10^4 PFU of WT ($n = 14$ mice), Omi-S ($n = 14$ mice) and Omicron ($n = 14$ mice). Lung samples of the infected mice were collected at 2 or 4 dpi to determine the viral titre ($n = 4$ mice) (**d**) or for immunohistochemistry (IHC)

detection of the N protein ($n = 3$ mice) (**e**). In **e**, representative IHC images showing SARS-CoV-2 N (brown colour) in alveoli (arrows) and bronchioles (arrowheads) in mice lungs at 2 dpi are presented. Scale bars, 100 μm. **f**, Percentage of N-positive bronchioles in the lungs of infected mice ($n = 3$ mice) at 2 dpi. Each dot represents an infected mouse. Statistical significance was determined using a two-tailed, unpaired t-test with Welch's correction (**a,b,d,f**) and log-rank (Mantel-Cox) test (**c**). $*P < 0.05$, $**P < 0.01$, $***P < 0.001$ and $****P < 0.0001$; NS, not significant.

chimeric viruses, each containing Omicron S in combination with one non-spike protein of Omicron, with the remaining proteins coming from WT virus (Extended Data Fig. 9b). When we combined Omicron S with Omicron nsp6 (Omi-S/nsp6), we observed a strong decrease in viral replication, with infection kinetics mimicking those of Omicron in cell culture (Fig. 3a–d); no such decrease was seen for other chimeric viruses. Poor replication efficiency of Omi-S/nsp6 was also corroborated by our finding that both Omi-S/nsp6 and Omicron took almost five to six days to recover by CPER, whereas all other variants were recovered in two days (data not shown). Finally, like Omicron, Omi-S/nsp6 was clearly outcompeted by Omi-S in a direct competition assay (Fig. 3e).

In lungs of K18-hACE2 mice, whereas Omi-S caused extensive bronchiolar infection and injury, both Omicron and Omi-S/nsp6 showed decreased infection with no evidence of epithelial damage (Fig. 3f). Consistent with these findings, lungs of Omi-S/nsp6-infected mice produced viral titres equivalent to those seen for rOmicron and Omicron isolate (Fig. 3g). Finally, 71% of mice infected with Omi-S/nsp6 survived (Fig. 3h)—in contrast with the survival rates of only 20% that were observed in mice infected with Omi-S (Fig. 2c). Overall, these results indicate that mutations in S and nsp6 are sufficient to define Omicron's attenuated virulence. These observations support and further extend the findings of a previous study showing that mutations
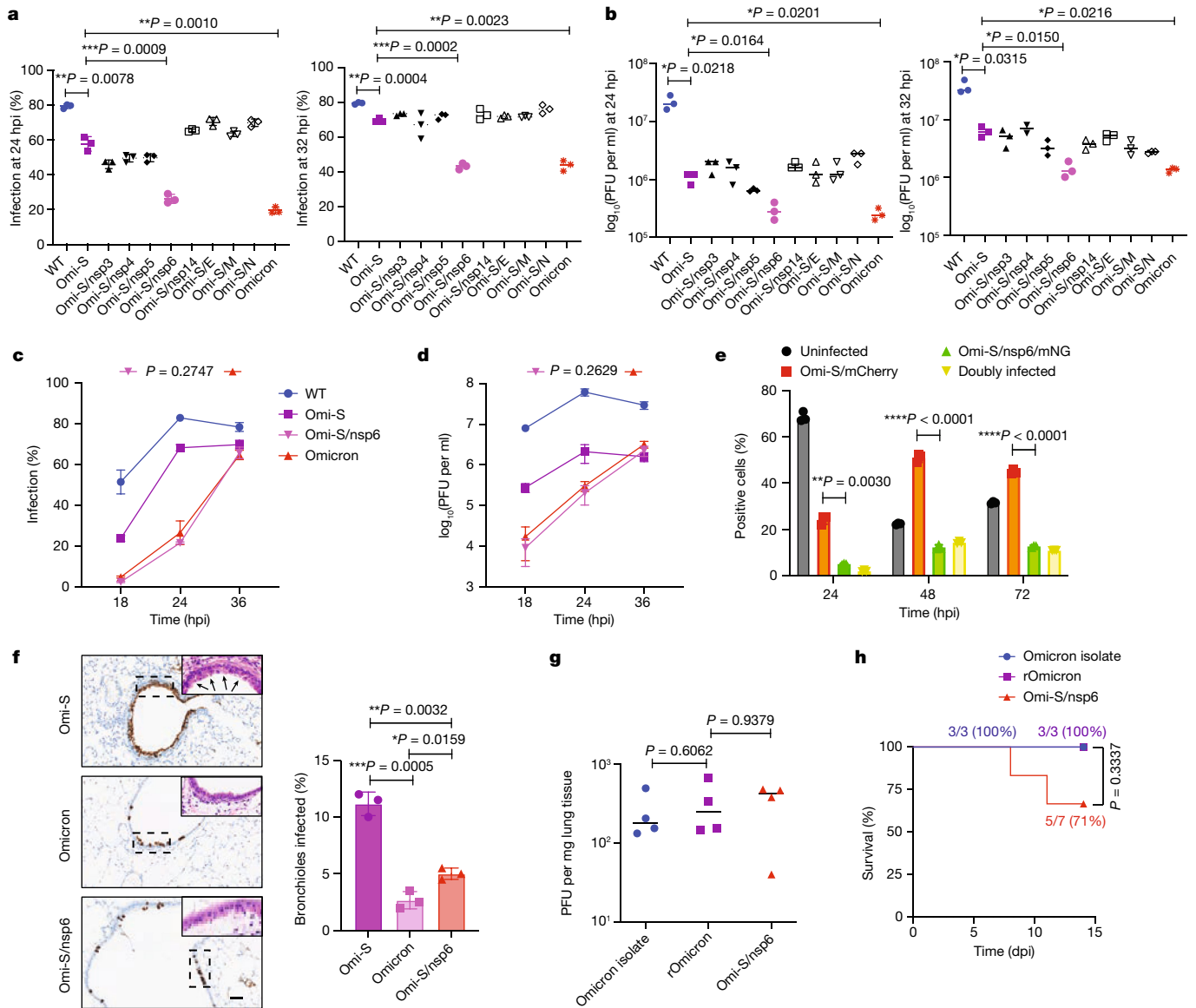
Fig. 3 | Mutations in S and nsp6 drive Omicron pathogenicity. a–d, Replication kinetics of indicated mNeonGreen reporter viruses in ACE2/TMPRSS2/Caco-2 cells (MOI = 0.01) determined by flow cytometry (n = 3 replicates) (**a,c**) and plaque assay (n = 3 replicates) (**b,d**). Experiments were repeated twice. **e,** ACE2/TMPRSS2/Caco-2 cells were infected with virus mixtures at a 1:1 ratio to obtain the final MOI of 0.005 for each virus. The cells were fixed at the indicated times and analysed by flow cytometry. Percentage of uninfected, singly infected and doubly infected cells is shown. Singly infected cells were used for compensation. Individual data points are plotted along with the mean ± s.d. (n = 3 replicates). The experiment was repeated twice. **f–h,** K18-hACE2 mice were intranasally inoculated with 1 × 10⁴ PFU of viruses. Lung samples of infected mice were collected at 2 dpi for IHC detection of the N protein (n = 3 mice) (**f**) or for determination of viral titres (n = 4 mice) (**g**). In **f,** representative images of H&E staining of N-positive bronchioles are shown in insets. Bronchiolar epithelial necrosis is indicated with arrows. No evidence of necrosis was seen in bronchioles of mice infected with Omicron or Omi-S/nsp6. Scale bar, 100 μm. The right graph in **f** shows the percentage of N-positive bronchioles in the lungs of infected mice. Each dot represents an infected mouse. **h,** Survival of infected mice monitored daily for 14 days. Mice that lost 20% of their initial body weight were euthanized. Statistical significance was determined using a two-tailed, unpaired *t*-test with Welch's correction (**a–g**) and log-rank (Mantel–Cox) test (**h**). *P < 0.05, **P < 0.01, ***P < 0.001 and ****P < 0.0001; NS, not significant.

in the 5′-UTR–nsp12 region, in which nsp6 resides, contribute to Omicron's attenuation in K18-hACE2 mice[30].

The S protein RBM drives Omicron's vaccine escape

A large body of literature has provided evidence of the extensive escape of Omicron from vaccine-induced humoral immunity[14,19]. To define S regions that are associated with the immune-escape phenotype of Omicron, we first compared the in vitro neutralization activity of sera from vaccinated individuals against WT SARS-CoV-2 (USA-WA1/2020),

Omi-S and Omicron. Sera collected within two months of the second dose of mRNA-1273 (Moderna mRNA vaccine; n = 12) or BNT162b2 (Pfizer-BioNTech mRNA vaccine; n = 12) vaccine were included (Extended Data Table 1). We performed a multicycle neutralization assay using a setting in which the virus and neutralizing sera were present at all times, mimicking the situation in a seropositive individual. All sera poorly neutralized Omicron, with an 11.1-fold (range: 4.4-fold to 81.2-fold; P < 0.0001) lower half-maximal neutralizing dilution (ND₅₀) for Omicron compared with WA1 (Fig. 4a,b). In fact, around 80% of samples did not completely neutralize Omicron at the highest tested
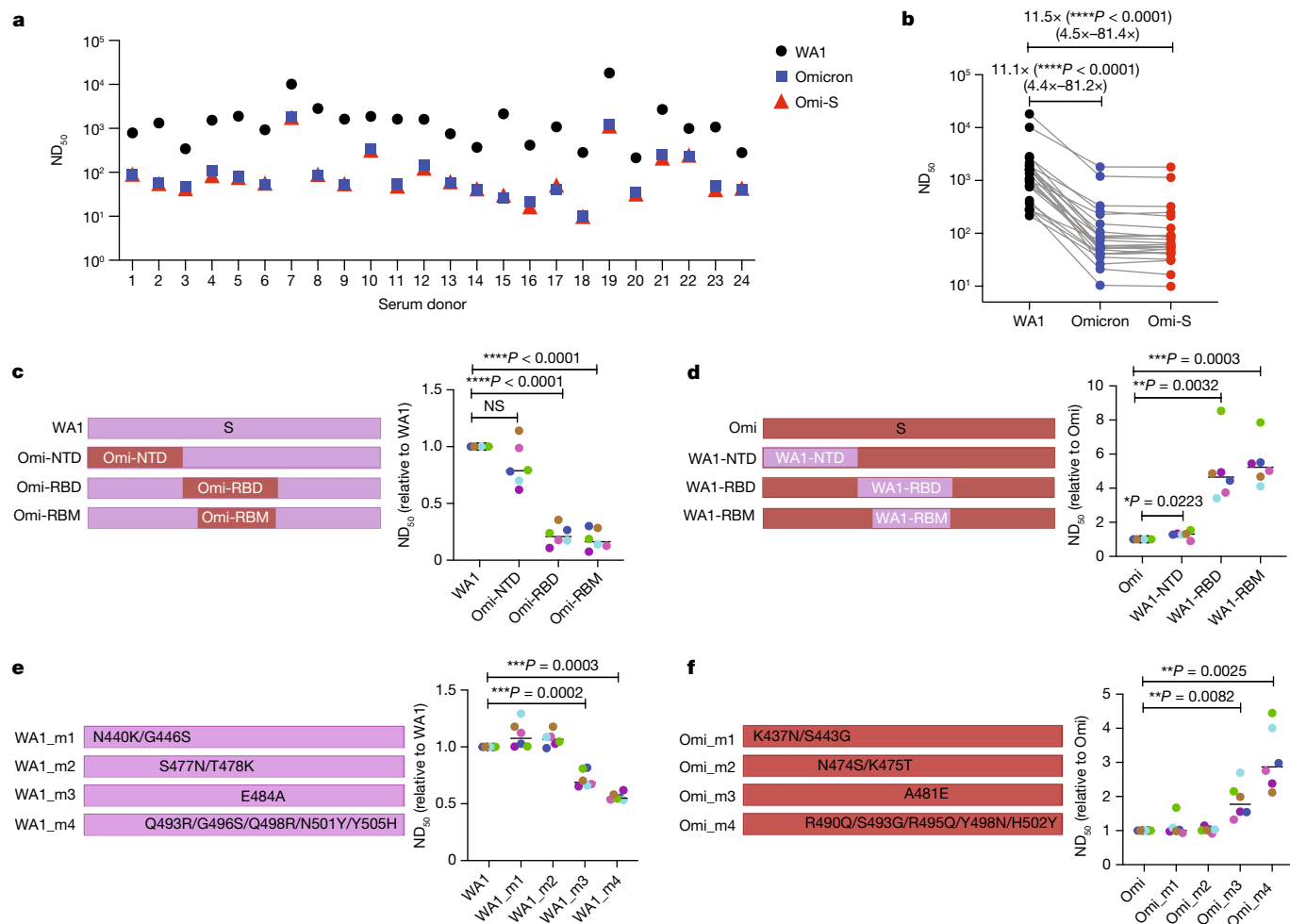
Fig. 4 | Role of S in the immune resistance of Omicron. a, ND_{50} values for WA1, Omi-S and Omicron in sera from individuals who received two shots of Moderna (donors 1–12) or Pfizer (donors 13–24) vaccine (further details of sera are provided in Extended Data Table 1; individual curves are shown in Extended Data Fig. 10). **b**, Trajectories of ND_{50} values against WA1, Omi-S and Omicron (the data from **a** are plotted). The fold change in ND_{50} values is indicated (n = 24 serum samples). **c–f**, Schematic of the chimeric (left; **c**,**d**) and mutant (left; **e**,**f**)

viruses. The amino acid numbering for WA1 mutants in **e** is based on the WA1 S sequence, whereas the numbering for Omicron mutants in **f** is based on the Omicron S sequence. Six of the 24 sera (3 from Moderna and 3 from Pfizer) were tested. Each serum sample is represented by a dot of specific colour. The data are plotted as the fold change of the parental virus. Statistical significance was determined using a two-tailed, unpaired t-test with Welch's correction. *P < 0.05, **P < 0.01, ***P < 0.001 and ****P < 0.0001; NS, not significant.

concentration (Extended Data Fig. 10). Notably, Omi-S exhibited identical ND_{50} values to Omicron (11.5-fold lower than that of WA1; P < 0.0001) (Fig. 4a,b), suggesting that the Omicron S protein, when incorporated into a WT virus, behaves the same way as it does in Omicron.

The SARS-CoV-2 S protein comprises two domains: the S1 domain, which interacts with the ACE2 receptor, and the S2 domain, which is responsible for membrane fusion[32]. Within the S1 domain lie an N-terminal domain (NTD) and a receptor-binding domain (RBD), which contains the receptor-binding motif (RBM) that makes direct contact with the ACE2 receptor[33]. The NTD of Omicron S has 11 amino acid changes, including 6 deletions and one 3-amino-acid-long insertion, whereas the RBD contains 15 mutations, 10 of which are concentrated in the RBM (Extended Data Fig. 1). Both the NTD and the RBD host neutralizing epitopes[34–37], but the RBD is immunodominant and represents the primary target of the neutralizing activity that is present in SARS-CoV-2 immune sera[37,38]. To determine whether the neutralization resistance phenotype of Omicron is caused by mutations in a particular domain of the S protein, we generated two groups of chimeric viruses. The first group comprised the WA1 virus carrying the NTD, RBD or RBM of Omicron (Fig. 4c), and the second group consisted of Omi-S virus bearing the NTD, RBD or RBM of WA1 (Fig. 4d). The neutralization assay showed

that mutations in the RBM were the main cause of Omicron's resistance to vaccine-induced humoral immunity: replacing the RBM of WA1 with that of Omicron decreased the ND_{50} by 5.4-fold (P < 0.0001) and, conversely, substituting the RBM of Omi-S with that of WA1 increased the ND_{50} by 5.6-fold (P = 0.0003) (Fig. 4c,d). The fact that none of the RBM-swap viruses achieved the difference of around 11-fold that was seen between WA1 and Omi-S suggests that mutations in other parts of S also contribute to vaccine resistance.

To investigate whether specific mutations in Omicron RBM drive vaccine escape, we generated two additional panels of recombinant viruses, one with WA1 S carrying Omicron RBM mutations, either singly or in combination (Fig. 4e), and the other with Omicron S lacking the same set of mutations (Fig. 4f). Two WA1 mutants—mutant 3 (with an E484A substitution) and mutant 4 (bearing a cluster of five substitutions Q493R, G496S, Q498R, N501Y and Y505H)—exhibited a moderate but statistically significant decrease of 1.4-fold (P = 0.0002) and 1.8-fold (P = 0.0003) in ND_{50} values, respectively, compared with WA1 (Fig. 4e). The opposite was observed when these mutations were removed from Omicron S; the Omicron mutant 3 (lacking the E484A substitution) and mutant 4 (lacking Q493R, G496S, Q498R, N501Y and Y505H) had 1.9-fold (P = 0.0082) and 3.1-fold (P = 0.0025) higher ND_{50} values

compared with Omicron (Fig. 4f). As none of the mutants captured the overall phenotype of Omicron, we assume that the vaccine escape is a cumulative effect of mutations distributed along the length of the S protein. It is possible that mutations alter the conformation of Omicron S in such a manner that most of the immunodominant neutralizing epitopes are disrupted and become unavailable for neutralization.

Discussion

This study provides key insights into viral proteins that contribute to SARS-CoV-2 pathogenicity. We show that S, the most mutated protein in Omicron, has an incomplete role in Omicron attenuation. In cell-based infection assays, the Omi-S virus exhibits an intermediate replication efficiency between the ancestral virus and Omicron. Similarly, in K18-hACE2 mice, Omi-S contrasts with non-fatal Omicron and leads to 80% mortality; the ancestral virus causes 100% mortality in these mice. Notably, when we combined S mutations with mutations in nsp6, the virus exhibited an attenuated phenotype largely resembling that of Omicron, indicating that these two proteins are major determinants of Omicron pathogenicity. Future studies will decipher the mechanism(s) by which nsp6 mutations affect viral replication.

One potential limitation of our study is the use of K18-hACE2 mice for pathogenesis studies instead of primate models that have more similarities with humans[39]. It should however be noted that K18-hACE2 mice are a well-established model for investigating the lethal phenotype of SARS-CoV-2[4,31]. Although these mice develop lung pathology after SARS-CoV-2 infection, mortality has been associated with involvement of the central nervous system owing to viral neuroinvasion and dissemination[31,40]. The fact that infection of K18-hACE2 mice with Omi-S, but not with Omicron, elicits neurological signs (for example, hunched posture and a lack of responsiveness) suggests that the neuroinvasion property is preserved in Omi-S, probably as a result of its higher replication efficiency, and that the determinants of this property lie outside of the S protein. These findings are consistent with a previous study showing that hamsters infected with Omi-S shed significantly more virus and lost more weight than those infected with Omicron, suggesting that mutations outside of S contribute to the attenuated pathogenicity of Omicron[41].

We found that although the ancestral virus mainly replicates in lung alveoli and causes only rare infection of bronchioles in K18-hACE2 mice, both Omi-S and Omicron exhibit an increased propensity to replicate in bronchiolar epithelium, indicating that the S protein is accountable for the changed tropism. The mechanism behind this switch is unknown, but it is possible that Omicron S is more efficient than WT S in using cathepsin B or cathepsin L (refs. [25,42,43]), which form an active viral entry pathway in bronchioles and other airway cells[41]. By contrast, the entry of SARS-CoV-2 into alveolar epithelial cells is mainly driven by TMPRSS2 (refs. [28,44]), which Omicron S is deficient in utilizing[25,45], leading to poor infection of these cells[4,5,25,43]. These findings may explain the attenuated lung pathology caused by Omicron.

Omicron nsp6 has two altered sites relative to the prototype SARS-CoV-2 Wuhan-Hu-1 isolate: a three-amino-acid deletion (LSG, positions 105–107) and an I189V substitution (Extended Data Fig. 9). Several functions of nsp6 in coronavirus replication have been described; chief among them is the biogenesis of double-membrane vesicles (DMVs), which represent the site of viral RNA synthesis[46–50]. A previous study showed that SARS-CoV-2 DMVs are mainly generated by the concerted action of three viral proteins: nsp3, nsp4, and nsp6; although nsp3 and nsp4 are sufficient for the formation of DMVs, nsp6 connects these DMVs with the endoplasmic reticulum and channelizes the essential communication between these structures[46]. Whether the constellation of mutations in Omicron nsp6 affects the formation or functions of DMVs needs further investigation. Nsp6 also activates NLR3-dependent cytokine production and pyroptosis in the lungs of patients with COVID-19, serving as a key virulence factor[47]. Of note, an nsp6 variant that is associated with asymptomatic COVID-19 exhibited a reduced ability to induce pyroptosis[47], prompting speculation that mutations in Omicron nsp6 may also influence pyroptosis. Detailed mechanistic studies will be required to dissect the effect of Omicron mutations on the functions of nsp6.

It is at present unknown whether mutations in S and nsp6 work in concert with each other to drive Omicron attenuation. Given that Omicron S showed a higher predilection for bronchioles, it is possible that S is responsible for the altered viral tropism, whereas non-spike mutations—including those in nsp6—are mere adaptations to the changed tissue environment. It is worth mentioning that although nsp6 seems to be the major non-spike protein behind Omicron attenuation, the contribution of other viral proteins cannot be completely ruled out. In vitro experiments examining the role of non-spike mutations were all carried out in ACE2/TMPRSS2/Caco-2 cells. Using other, more immune-competent cell types could reveal the effect of other non-spike mutations as well. In addition, our chimeric viruses contained Omicron S paired with only one non-spike protein at a time, which limited long-range epistatic interactions between mutations in multiple viral proteins.

Our study shows that mutations in the RBM of Omicron S are the main determinants of Omicron's escape from neutralizing antibodies, although mutations in other regions of S also contribute. Within the RBM, we identify two hotspots of mutations, which give Omicron S the ability to resist neutralization: one bearing the E484A substitution and the other containing a cluster of five substitutions—Q493R, G496S, Q498R, N501Y and Y505H. The E484A substitution has been shown to escape neutralization by convalescent sera[51]. Moreover, structural modelling suggests that some therapeutic monoclonal antibodies establish highly stable salt bridges with the E484 residue, entirely losing their binding when this residue is changed to A or after Q493K and Y505H changes[52]. Similarly, mapping of RBM residues that directly interact with 49 known neutralizing antibodies revealed N440, G446, S477 and T478 as low-frequency interactors, N501, Y505 and Q498 as medium-frequency interactors and E484 and Q493 as high-frequency interactors[53], in line with our neutralization assay results. Notably, although the antibody-binding potential of Omicron S is impaired[54], its receptor-binding capacity is intact. In fact, the Omicron RBD has a higher affinity for ACE2 relative to the Wuhan-Hu-1 and Delta RBDs[25]. This indicates that mutations in Omicron S have evolved in such a manner that they hinder antibody binding but preserve the receptor engagement. This opens up the possibility of targeting the conserved and structurally constrained regions of S that are involved in ACE2 recognition for the design of broad-spectrum vaccines to control the COVID-19 pandemic.

Online content

Any methods, additional references, Nature Portfolio reporting summaries, source data, extended data, supplementary information, acknowledgements, peer review information; details of author contributions and competing interests; and statements of data and code availability are available at https://doi.org/10.1038/s41586-023-05697-2.

1. Liu, L. et al. Striking antibody evasion manifested by the Omicron variant of SARS-CoV-2. *Nature* **602**, 676–681 (2022).
2. Planas, D. et al. Considerable escape of SARS-CoV-2 Omicron to antibody neutralization. *Nature* **602**, 671–675 (2022).
3. Schmidt, F. et al. Plasma neutralization of the SARS-CoV-2 Omicron variant. *N. Engl. J. Med.* **386**, 599–601 (2022).
4. Shuai, H. et al. Attenuated replication and pathogenicity of SARS-CoV-2 B.1.1.529 Omicron. *Nature* **603**, 693–699 (2022).
5. Halfmann, P. J. et al. SARS-CoV-2 Omicron virus causes attenuated disease in mice and hamsters. *Nature* **603**, 687–692 (2022).
6. Lewnard, J. A. et al. Clinical outcomes associated with SARS-CoV-2 Omicron (B.1.1.529) variant and BA.1/BA.1.1 or BA.2 subvariant infection in Southern California. *Nat. Med.* **28**, 1933–1943 (2022).

Article

7. Wolter, N. et al. Early assessment of the clinical severity of the SARS-CoV-2 omicron variant in South Africa: a data linkage study. *Lancet* **399**, 437–446 (2022).
8. Ulloa, A. C., Buchan, S. A., Daneman, N. & Brown, K. A. Estimates of SARS-CoV-2 Omicron variant severity in Ontario, Canada. *J. Am. Med. Assoc.* **327**, 1286–1288 (2022).
9. Uraki, R. et al. Characterization of SARS-CoV-2 Omicron BA.4 and BA.5 isolates in rodents. *Nature* **612**, 540–545 (2022).
10. Uraki, R. et al. Characterization and antiviral susceptibility of SARS-CoV-2 Omicron BA.2. *Nature* **607**, 119–127 (2022).
11. Dyer, O. Covid-19: Omicron is causing more infections but fewer hospital admissions than delta, South African data show. *Br. Med. J.* **375**, n3104 (2021).
12. Sigal, A. Milder disease with Omicron: is it the virus or the pre-existing immunity? *Nat. Rev. Immunol.* **22**, 69–71 (2022).
13. WHO. Tracking SARS-CoV-2 variants https://www.who.int/en/activities/tracking-SARS-CoV-2-variants/ (2022).
14. Cele, S. et al. Omicron extensively but incompletely escapes Pfizer BNT162b2 neutralization. *Nature* **602**, 654–656 (2022).
15. Gu, H. et al. Probable transmission of SARS-CoV-2 omicron variant in quarantine hotel, Hong Kong, China, November 2021. *Emerg. Infect. Dis.* **28**, 460–462 (2022).
16. Iuliano, A. D. et al. Trends in disease severity and health care utilization during the early Omicron variant period compared with previous SARS-CoV-2 high transmission periods—United States, December 2020–January 2022. *Morb. Mortal. Wkly Rep.* **71**, 146–152 (2022).
17. CDC. COVID Data Tracker https://covid.cdc.gov/covid-data-tracker/#variant-proportions (2022).
18. Taylor, L. Covid-19: Omicron drives weekly record high in global infections. *Br. Med. J.* **376**, o66 (2022).
19. Dejnirattisai, W. et al. SARS-CoV-2 Omicron-B.1.1.529 leads to widespread escape from neutralizing antibody responses. *Cell* **185**, 467–484 (2022).
20. Suzuki, R. et al. Attenuated fusogenicity and pathogenicity of SARS-CoV-2 Omicron variant. *Nature* **603**, 700–705 (2022).
21. Smyth, D. S. et al. Tracking cryptic SARS-CoV-2 lineages detected in NYC wastewater. *Nat. Commun.* **13**, 635 (2022).
22. Kirby, A. E. et al. Notes from the field: early evidence of the SARS-CoV-2 B.1.1.529 (Omicron) variant in community wastewater—United States, November–December 2021. *Morb. Mortal. Wkly Rep.* **71**, 103–105 (2022).
23. Herrmann, A. et al. Cloning of a passage-free SARS-CoV-2 genome and mutagenesis using red recombination. *Int. J. Mol. Sci.* **22**, 10188 (2021).
24. Liu, G. & Gack, M. U. An optimized circular polymerase extension reaction-based method for functional analysis of SARS-CoV-2. Preprint at https://doi.org/10.1101/2022.11.26.518005 (2022).
25. Meng, B. et al. Altered TMPRSS2 usage by SARS-CoV-2 Omicron impacts tropism and fusogenicity. *Nature* **603**, 706–714 (2022).
26. Willett, B. J. et al. SARS-CoV-2 Omicron is an immune escape variant with an altered cell entry pathway. *Nat. Microbiol.* **7**, 1161–1179 (2022).
27. Martines, R. B. et al. Pathology and pathogenesis of SARS-CoV-2 associated with fatal coronavirus disease, United States. *Emerg. Infect. Dis.* **26**, 2005–2015 (2020).
28. Huang, J. et al. SARS-CoV-2 infection of pluripotent stem cell-derived human lung alveolar type 2 cells elicits a rapid epithelial-intrinsic inflammatory response. *Cell Stem Cell* **27**, 962–973 (2020).
29. Mulay, A. et al. SARS-CoV-2 infection of primary human lung epithelium for COVID-19 modeling and drug discovery. *Cell Rep.* **35**, 109055 (2021).
30. Liu, S., Selvaraj, P., Sangare, K., Luan, B. & Wang, T. T. Spike protein-independent attenuation of SARS-CoV-2 Omicron variant in laboratory mice. *Cell Rep.* **40**, 111359 (2022).
31. Carossino, M. et al. Fatal neurodissemination and SARS-CoV-2 tropism in K18-hACE2 mice is only partially dependent on hACE2 expression. *Viruses* **14**, 535 (2022).
32. Huang, Y., Yang, C., Xu, X. F., Xu, W. & Liu, S. W. Structural and functional properties of SARS-CoV-2 spike protein: potential antivirus drug development for COVID-19. *Acta Pharmacol. Sin.* **41**, 1141–1149 (2020).
33. Lan, J. et al. Structure of the SARS-CoV-2 spike receptor-binding domain bound to the ACE2 receptor. *Nature* **581**, 215–220 (2020).
34. Chi, X. et al. A neutralizing human antibody binds to the N-terminal domain of the Spike protein of SARS-CoV-2. *Science* **369**, 650–655 (2020).
35. Voss, W. N. et al. Prevalent, protective, and convergent IgG recognition of SARS-CoV-2 non-RBD spike epitopes. *Science* **372**, 1108–1112 (2021).
36. Premkumar, L. et al. The receptor binding domain of the viral spike protein is an immunodominant and highly specific target of antibodies in SARS-CoV-2 patients. *Sci. Immunol.* **5**, eabc8413 (2020).
37. Ju, B. et al. Human neutralizing antibodies elicited by SARS-CoV-2 infection. *Nature* **584**, 115–119 (2020).
38. Piccoli, L. et al. Mapping neutralizing and immunodominant sites on the SARS-CoV-2 spike receptor-binding domain by structure-guided high-resolution serology. *Cell* **183**, 1024–1042 (2020).
39. Chang, M. C., Hild, S. & Grieder, F. Nonhuman primate models for SARS-CoV-2 research: consider alternatives to macaques. *Lab Anim.* **50**, 113–114 (2021).
40. Kumari, P. et al. Neuroinvasion and encephalitis following intranasal inoculation of SARS-CoV-2 in K18-hACE2 mice. *Viruses* **13**, 132 (2021).
41. Peacock, T. P. et al. The altered entry pathway and antigenic distance of the SARS-CoV-2 Omicron variant map to separate domains of spike protein. Preprint at https://doi.org/10.1101/2021.12.31.474653 (2022).
42. Padmanabhan, P. & Dixit, N. M. Modelling how the altered usage of cell entry pathways by the SARS-CoV-2 Omicron variant may affect the efficacy and synergy of TMPRSS2 and cathepsin B/L inhibitors. Preprint at https://doi.org/10.1101/2022.01.13.476267 (2022).
43. Hui, K. P. Y. et al. SARS-CoV-2 Omicron variant replication in human bronchus and lung ex vivo. *Nature* **603**, 715–720 (2022).
44. Grau-Exposito, J. et al. Evaluation of SARS-CoV-2 entry, inflammation and new therapeutics in human lung tissue cells. *PLoS Pathog.* **18**, e1010171 (2022).
45. Zhao, H. et al. SARS-CoV-2 Omicron variant shows less efficient replication and fusion activity when compared with Delta variant in TMPRSS2-expressed cells. *Emerg. Microbes Infect.* **11**, 277–283 (2022).
46. Ricciardi, S. et al. The role of NSP6 in the biogenesis of the SARS-CoV-2 replication organelle. *Nature* **606**, 761–768 (2022).
47. Sun, X. et al. SARS-CoV-2 non-structural protein 6 triggers NLRP3-dependent pyroptosis by targeting ATP6AP1. *Cell Death Differ.* **29**, 1240–1254 (2022).
48. Cottam, E. M., Whelband, M. C. & Wileman, T. Coronavirus NSP6 restricts autophagosome expansion. *Autophagy* **10**, 1426–1441 (2014).
49. Benvenuto, D. et al. Evolutionary analysis of SARS-CoV-2: how mutation of non-structural protein 6 (NSP6) could affect viral autophagy. *J. Infect.* **81**, e24–e27 (2020).
50. Gosert, R., Kanjanahaluethai, A., Egger, D., Bienz, K. & Baker, S. C. RNA replication of mouse hepatitis virus takes place at double-membrane vesicles. *J. Virol* **76**, 3697–3708 (2002).
51. Liu, Z. et al. Identification of SARS-CoV-2 spike mutations that attenuate monoclonal and serum antibody neutralization. *Cell Host Microbe* **29**, 477–488 (2021).
52. Shah, M. & Woo, H. G. Omicron: a heavily mutated SARS-CoV-2 variant exhibits stronger binding to ACE2 and potently escapes approved CO VID-19 therapeutic antibodies. *Front. Immunol.* **12**, 830527 (2021).
53. Ye, G., Liu, B. & Li, F. Cryo-EM structure of a SARS-CoV-2 omicron spike protein ectodomain. *Nat. Commun.* **13**, 1214 (2022).
54. Carreno, J. M. et al. Activity of convalescent and vaccine serum against SARS-CoV-2 Omicron. *Nature* **602**, 682–688 (2022).

Methods

Cells, antibodies and plasmids

The cell lines were incubated at 37 °C and 5% CO_2 in a humidified incubator. Human embryonic kidney HEK293T cells (ATCC; CRL-3216), human lung adenocarcinoma A549 cells (ATCC; CCL-185), human colorectal adenocarcinoma Caco-2 cells (ATCC; HTB-37) and African green monkey kidney Vero E6 cells were maintained in Dulbecco's modified Eagle's medium (DMEM) (Gibco; 11995-065) containing 10% fetal bovine serum (FBS) and 1× non-essential amino acids. A lentiviral delivery system was used to generate cells stably expressing human ACE2 and TMPRSS2. The mycoplasma-negative status of all cell lines was confirmed.

Anti-SARS-CoV N protein antibody (Rockland; 200-401-A50; 1:2,000) was used to detect the SARS-CoV-2 N protein by immunofluorescence and western blot. Mouse anti-SARS-CoV-2 spike antibody (GeneTex; GTX632604; 1:1,000), directed against the S2 subunit, was used for western blot analysis of S-protein cleavage in virus particles and infected cells.

Plasmids encoding various fragments of the SARS-CoV-2 genome (Hu/DP/Kng/19-020 isolate) were a gift from Y. Matsuura[55]. We replaced the S gene in the plasmid pCSII-SARS-CoV-2 F8 (ref. [55]) with the chemically synthesized Omicron S gene and named this plasmid pCSII-SARS-CoV-2 F8_Omicron. We replaced the open reading frame (ORF) 7 in the plasmid pcDNA3.1-SARS-CoV-2 F9+10 with mNeonGreen or mCherry to obtain plasmids pcDNA3.1-SARS-CoV-2 F9+10_mNG and pcDNA3.1-SARS-CoV-2 F9+10_mCherry, respectively. The plasmids pMW-CoV-2-UTRlinker (ref. [55]) and pGL-CPERlinker (ref. [24]), both containing a linker fragment comprising hepatitis delta virus ribozyme (HDVr), the bovine growth hormone polyadenylation signal sequence (BGH-polyA) and cytomegalovirus (CMV) promoter, have been previously reported. The lentiviral vectors, pLOC_hACE2_PuroR and pLOC_hTMPRSS2_BlastR, containing human ACE2 and TMPRSS2, respectively, have been described previously[56].

Biocontainment

All procedures were performed in a state-of-the-art biosafety level 3 (BSL3) facility at the National Emerging Infectious Diseases Laboratories (NEIDL) of Boston University using biosafety protocols approved by the Institutional Biosafety Committee (IBC). The experimental plans, including the generation of recombinant chimeric viruses, were reviewed and approved by the IBC, which comprises scientists, biosafety and compliance experts and members of the local community. Furthermore, the research was approved by the Boston Public Health Commission. All personnel received rigorous biosafety, biosecurity and BSL3 training before participating in experiments. Personal protective equipment, including scrubs, disposable overalls, shoe covers, double-layered gloves and powered air-purifying respirators, was used. Biosecurity measures are built in the environment through building and security systems and are reinforced through required training programmes, standing meetings and emergency exercises. The researchers involved in working with chimeric viruses received at least two booster shots of the SARS-CoV-2 mRNA vaccine before the study was started. Finally, all researchers were medically cleared by the Boston University Research Occupational Health Program.

Collection of serum samples

Sera from individuals who received two doses of mRNA-1273 (Moderna) or BNT162b2 (Pfizer) vaccine were collected at Boston Medical Center at least two weeks after the final dose. These individuals had no prior history of SARS-CoV-2 infection. Serum samples were collected using protocols reviewed and approved by the Institutional Review Board at Boston Medical Center. All methods were performed in accordance with relevant guidelines and regulations. The participants provided electronic informed consent. De-identified samples were used in this research. Additional information for serum samples is provided in Extended Data Table 1.

Omicron stock preparation and titration

The SARS-CoV-2 BA.1 Omicron virus stock was generated in ACE2/TMPRSS2/Caco-2 cells. In brief, 5×10^5 cells, grown overnight in DMEM, 10% FBS and 1× NEAA in one well of a six-well plate, were inoculated with the collection medium in which the nasal swab from a patient with COVID-19 was immersed. The swab material was obtained from the Department of Public Health, Massachusetts, and it contained the sequence-verified Omicron virus (NCBI accession number: OL719310). Twenty-four hours after infecting cells, the culture medium was replaced with 2 ml of DMEM, 2% FBS and 1× NEAA and the cells were incubated for another 72 h, at which point the CPE became visible. The culture medium was collected, passed through a 0.45 µm filter and kept at −80 °C as a P0 virus stock. To generate a P1 stock, we infected 1×10^7 ACE2/TMPRSS2/Caco-2 cells, seeded the day before in a T175 flask, with the P0 virus at an MOI of 0.01. The next day, the culture medium was changed to 25 ml of 2% FBS-containing medium. Three days later, when the cells exhibited excessive CPE, the culture medium was collected, passed through a 0.45 µm filter and stored at −80 °C as a P1 stock.

To titrate the virus stock, we seeded ACE2/TMPRSS2/Caco-2 cells into a 12-well plate at a density of 2×10^5 cells per well. The next day, the cells were incubated with serial 10-fold dilutions of the virus stock (250 µl volume per well) for 1 h at 37 °C, overlaid with 1 ml per well of medium containing a 1:1 mixture of 2× DMEM/4% FBS and 1.2% Avicel (DuPont; RC-581) and incubated at 37 °C for another three days. To visualize the plaques, the cell monolayer was fixed with 4% paraformaldehyde and stained with 0.1% crystal violet, with both fixation and staining performed at room temperature for 30 min each. The number of plaques was counted and the virus titre was calculated.

Generation of recombinant SARS-CoV-2 by CPER

SARS-CoV-2 recombinant viruses were generated using a previously described optimized CPER protocol[24]. Full-length SARS-CoV-2 cDNA cloned into a bacterial artificial chromosome (BAC)[23] was used to generate WT and Omi-S viruses. In brief, the BAC was amplified into eight overlapping fragments (F1, F2, F3, F4, F5, F6, F7 and F9) covering the whole SARS-CoV-2 genome. The pCSII-SARS-CoV-2 F8 (containing a D614G substitution) and pCSII-SARS-CoV-2 F8_Omicron plasmids, which were used to generate S mutants, served as templates for the amplification of fragment 8 (F8). The UTR linker plasmids pMW-CoV-2-UTRlinker (ref. [55]) or pGL-CPERlinker (ref. [24]) were used as a template to amplify the linker sequence. The 5′ termini of all ten DNA fragments (F1–F9 and the linker) were phosphorylated by using T4 PNK (NEB; M0201). The CPER reaction containing equimolar amounts (0.05 pmol) of each fragment was performed with PrimeStar GXL DNA polymerase (Takara Bio; R050A) as previously described[24]. The nicks in the circular product were sealed by using HiFi Taq DNA ligase (NEB; M0647S).

To generate chimeric viruses containing a combination of Omicron S and non-spike proteins (Omi-S/nsp3, Omi-S/nsp4, Omi-S/nsp5, Omi-S/nsp6, Omi-S/nsp14, Omi-S/E, Omi-S/M and Omi-S/N), we used SARS-CoV-2 plasmids described previously[55] as templates, provided by Y. Matsuura. These plasmids contained SARS-CoV-2 sequences derived from the SARS-CoV-2/Hu/DP/Kng/19-020 strain. We introduced mutations into these plasmids using the standard DNA recombination technology. Our chimeric viruses also contained a P323L substitution in nsp12. Plasmid sequences were confirmed by the Sanger method.

To transfect cells with the CPER product, we seeded ACE2/TMPRSS2/Caco-2 cells into a six-well plate at a density of 5×10^5 cells per well. The transfection mix was prepared by mixing 26 µl of the original 52-µl CPER reaction volume with 250 µl of Opti-MEM (Thermo Fisher Scientific; 31985070) and 6 µl of TransIT-X2 Dynamic Delivery System (Mirus Bio; MIR 6000). After incubation at room temperature for 25 min, the transfection mix was added to the cells. The next day, the culture medium was replaced with fresh DMEM containing 2% FBS. The CPE became visible in three to four days, at which point the culture medium was collected

and stored as a P0 virus stock. The P0 stock was used for experiments described in this manuscript. The sequence of CPER-generated viruses was confirmed by next-generation sequencing.

SARS-CoV-2 whole-viral sequencing and genome assembly

cDNA synthesis was performed using Superscript IV reverse transcriptase (Invitrogen). Whole-viral amplification was performed with the NEB Varskip protocol using multiplexed primer pools designed with Primal Scheme, generating 400-bp tiling amplicons. PCR products from the Varskip protocol were pooled together and Illumina library construction was performed using the Nextera XT Library Prep Kit (Illumina). Deep-sequencing data analysis was performed using the Stanford Coronavirus Antiviral & Resistance Database (CoV-RDB) platform[57]. Input FASTQ sequence alignment with the Wuhan-Hu-1 reference was done using MiniMap2 v.2.22 in the CodFreq pipeline (https://github.com/hivdb/codfreq). The output of MiniMap2, an aligned SAM file, was converted to a CodFreq file by a Python script written in-house, using a PySam library (v.0.18.0), and was further analysed with the CoV-RDB. SARS-COV-2 variant calling was done using CoV-RDB Scorpio call v.1.2.123 (ref. [58]) (https://pangolin.cog-uk.io/) and Nextclade v.1.13.2 (ref. [59]) (https://clades.nextstrain.org/). PCR and sequencing run were performed once with the appropriate positive and negative controls.

SARS-CoV-2 neutralization assay

For neutralization assays, initial 1:10 dilutions of plasma, obtained from individuals who received two shots of either the Moderna or the Pfizer mRNA-based SARS-CoV-2 vaccine, were fivefold serially diluted in Opti-MEM over seven or eight dilutions. These plasma dilutions were then mixed at a 1:1 ratio with 1.25×10^4 infectious units of SARS-CoV-2 and incubated for 1 h at 37 °C. Thereafter, 100 μl of this mixture was directly applied to ACE2/A549 cells seeded the previous day in poly-L-lysine-coated 96-well plates at a density of 2.5×10^4 cells per well in a volume of 100 μl. Thus, the final starting dilution of plasma was 1:20 and the final MOI was 0.5. The cells were incubated at 37 °C for 24 h, after which they were fixed and stained with an anti-N antibody. When PBS instead of plasma was used as a negative control, these infection conditions resulted in around 40–50% infected cells at 24 hpi.

Generation and infection of iAT2 cells

The detailed protocol for generation of human iPS-cell-derived alveolar epithelial type II cells (iAT2 cells) has been published in our previous papers[28,60]. The ALI cultures were established by preparing single-cell suspensions of iAT2 three-dimensional (3D) sphere cultures grown in Matrigel. In brief, Matrigel droplets containing iAT2 spheres were dissolved in 2 mg ml⁻¹ dispase (Sigma) and the spheres were dissociated in 0.05% trypsin (Gibco) to generate a single-cell suspension. Transwell inserts (6.5 mm; Corning) were coated with dilute Matrigel (Corning) in accordance with the manufacturer's protocol. Single-cell iAT2 cells were plated on Transwells at a density of 520,000 cells per cm² in 100 μl of CK+DCI medium containing 10 μM of rho-associated kinase inhibitor ("Y"; Sigma Y-27632). Six hundred microlitres of this medium was added to the basolateral compartment. Twenty-four hours after plating, the basolateral medium was changed with fresh CK+DCI+Y medium. Forty-eight hours after plating, the apical medium was aspirated to initiate the ALI culture. Seventy-two hours after plating, the basolateral medium was replaced with CK+DCI medium to remove the rho-associated kinase inhibitor. Basolateral medium was changed every two days thereafter. The detailed composition of CK+DCI medium is provided in our previous publications[28,60].

iAT2 cells in ALI cultures were infected with purified SARS-CoV-2 stock at an MOI of 2.5 based on the titration that was done on ACE2/TMPRSS2/Caco-2 cells. For infection, 100 μl of inoculum prepared in 1× PBS (or mock-infected with PBS only) was added to the apical chamber of each Transwell and incubated for 2 h at 37 °C, followed by the removal of the inoculum and washing of the apical side three times with 1× PBS (100 μl per wash). The cells were incubated for two or four days, after which the newly released virus particles on the apical side were collected by adding 100 μl of 1× PBS twice to the apical chamber and incubating at 37 °C for 15 min. The number of infectious virus particles in the apical washes was measured by the plaque assay on ACE2/TMPRSS2/Caco-2 cells. For flow cytometry, iAT2 cells were detached by adding 0.2 ml Accutase (Sigma; A6964) apically, and incubated at room temperature for 15 min. The detached cells were pelleted by low-speed centrifugation, fixed in 10% formalin and stained with anti-SARS-CoV-2 N antibody.

Detection of S-protein incorporation and cleavage in SARS-CoV-2 particles

The culture medium of ACE2/TMPRSS2/Caco-2 cells transfected with the CPER product was collected and passed through 0.22-μm filters. The SARS-CoV-2 particles were pelleted down by mixing an equal volume of the culture medium with 20% PEG6000 in PBS followed by overnight incubation at 4 °C. The mixture was centrifuged at 12,000g for 30 min at 4 °C, and the pellet was resuspended in 1× SDS sample buffer. The protein concentration was measured by the BCA assay using Pierce BCA Protein Assay kit (Thermo Fisher Scientific; 23225). Equal amounts of protein were resolved on 4–12% SDS page. The S protein was detected with mouse anti-SARS-CoV-2 spike antibody (GeneTex; GTX632604; 1:1,000) and IRDye 800CW donkey anti-mouse IgG secondary antibody (LI-COR Biosciences; 926-32212; 1:5,000). The bands were visualized by scanning the membrane with the LiCor CLx infrared scanner. The open-source package ImageJ (v.1.53a) was used to measure the intensity of protein bands.

Flow cytometry

For flow cytometry, fixed cells were permeabilized in 1× permeabilization buffer (Thermo Fisher Scientific; 00-5523-00) and stained with SARS-CoV-2 nucleocapsid antibody (Rockland; 200-401-A50, 1:1,000), followed by donkey anti-rabbit IgG-AF647 secondary antibody (Thermo Fisher Scientific; A-31573). Cells infected with fluorescent reporter viruses were fixed and analysed without staining. Gating was based on uninfected, stained control cells. The extent of staining was quantified using a BD LSR II flow cytometer (BD Biosciences), and the data were analysed with FlowJo v.10.6.2 (FlowJo, Tree Star). The gating strategy for flow cytometry is shown in Supplementary Fig. 1.

Immunofluorescence

Immunofluorescence was performed as described in our previous publication[56]. In brief, virus-infected cells were fixed in 4% paraformaldehyde and permeabilized in a buffer containing 0.1% Triton X-100 prepared in PBS. After blocking in a buffer containing 0.1% Triton X-100, 10% goat serum and 1% BSA, the cells were incubated overnight at 4 °C with anti-SARS-CoV N antibody (1:2,000 dilution). The cells were then stained with Alexa Fluor 568-conjugated goat anti-rabbit secondary antibody (1:1,000 dilution) (Invitrogen; A11008) in the dark at room temperature for 1 h and counterstained with DAPI. Images were captured using the ImageXpress Micro Confocal (IXM-C) High-Content Imaging system (Molecular Devices) with a 4× S Fluor objective lens at a resolution of 1.7 μm per pixel in the DAPI (excitation, 400 nm/40 nm; emission, 447 nm/60 nm) and TexasRed (excitation, 570 nm/80 nm; emission, 624 nm/40 nm) channels. Both channels were used to establish their respective laser autofocus offsets. The images were analysed using MetaXpress High Content Image Acquisition and Analysis software (Molecular Devices). First, the images were segmented using the CellScoring module. The objects between 7 μm and 20 μm in diameter and greater than 1,800 grey level units in intensity were identified and classified as nuclei. Positive cells were taken as nuclei having a Texas-Red signal of 1,500 grey level units or above within 10–20 μm of each nucleus. The remaining objects were set to negative cells. From these

objects, the following readouts were measured and used for downstream analysis: total number of positive and negative cells; total area of positive cells; and integrated intensity in the TexasRed channel for positive cells. To calculate the ND_{50}, we performed a non-linear regression curve fit analysis using Prism 9 software (GraphPad).

Mice maintenance and approvals

Mice were maintained in a facility accredited by the Association for the Assessment and Accreditation of Laboratory Animal Care (AAALAC). Animal studies were performed following the recommendations in the Guide for the Care and Use of Laboratory Animals of the National Institutes of Health. The protocols were approved by the Boston University Institutional Animal Care and Use Committee (IACUC). Heterozygous K18-hACE2 C57BL/6J mice (Strain 2B6.Cg-Tg(K18-ACE2)2Prlmn/J) were purchased from the Jackson Laboratory (JAX). Mice were housed in groups of four or five in ventilated cages (Tecniplast) and maintained on a 12:12 light cycle at 30–70% humidity, 20 °C temperature, ad libitum water and ad libitum standard chow diet (LabDiet).

Mice infection

Male and female K18-hACE2 mice (12–20 weeks old) were inoculated intranasally with 10^4 PFU of SARS-CoV-2 in 50 μl of sterile 1× PBS. The inoculations were performed under 1–3% isoflurane anaesthesia. In vivo experiments were not blinded, and mice were randomly assigned to infection groups. No a priori sample size calculation was performed. Instead, samples sizes were determined on the basis of our previous animal work. Twenty-six mice (6 for WT, 10 for Omi-S and 10 for Omicron) were enrolled in a 14-day survival study, and another 42 mice (14 for each of the WT, Omi-S and Omicron viruses) were used for virological and histological analysis of infected lungs. During the survival study, the mice were monitored for body weight, respiration, general appearance, responsiveness and neurological signs. An IACUC-approved clinical-scoring system was used to monitor disease progression and define humane end-points. The score of 1 was given for each of the following situations: body weight, 10–19% loss; respiration, rapid and shallow with increased effort; appearance, ruffled fur and/or hunched posture; responsiveness, low to moderate unresponsiveness; and neurological signs, tremors. The sum of these individual scores constituted the final clinical score. Mice were considered moribund and humanly euthanized in case of weight loss greater than or equal to 20%, or if they received a clinical score of 4 or above for two consecutive days. Body weight and clinical score were recorded once per day for the duration of the study. For the purpose of survival curves, mice euthanized on a given day were counted dead the day after. Mice that were found dead in the cage were counted dead on the same day. For euthanasia, an overdose of ketamine was administered followed by a secondary method of euthanasia.

For the quantification of SARS-CoV-2 infectious particles in lungs by plaque assay, lung tissues were collected in 600 μl of RNAlater stabilization solution (Thermo Fisher Scientific; AM7021) and stored at −80 °C until analysis. Twenty to forty milligrams of tissue was placed in a tube containing 600 μl of Opti-MEM and a 5-mm stainless steel bead (Qiagen; 69989) and homogenized in the Qiagen TissueLyser II by two dissociation cycles (1,800 oscillations per min for 2 min) with a 1-min interval between cycles. The homogenate was centrifuged at 15,000g for 10 min at room temperature and the supernatant was transferred to a new tube. Tenfold serial dilutions of this supernatant were used for the plaque assay on ACE2/TMPRSS2/Caco-2 cells, as described above.

For IHC and histological analysis, the insufflated whole lung tissues were inactivated in 10% neutral buffered formalin at a 20:1 fixative-to-tissue ratio for a minimum of 72 h before removal from BSL3 in accordance with an approved IBC protocol. Tissues were subsequently processed and embedded in paraffin, and 5-μm sections were stained with H&E following standard histological procedures.

IHC was performed using a Ventana BenchMark Discovery Ultra autostainer (Roche Diagnostics). An anti-SARS-CoV-2 S antibody (Cell Signaling Technologies; clone E5S3V) or anti-SARS-CoV-2 N antibody (Cell Signaling Technologies; clone 1C7C7) that showed equivalent immunoreactivity against WT and Omicron proteins was used to identify virus-infected cells. For the SARS-CoV-2 N antibody, given its mouse origin, an additional rabbit anti-mouse anti-Ig1 + Ig2a + IgG3 antibody (Abcam; 133469) was used to prevent non-specific binding. A HRP-conjugated goat anti-rabbit IgG polymer detection was then used to detect the viral specific antibodies (Vector Laboratories; MP-7451) and finally developed using 3,3′-diaminobenzidine (DAB) chromogen and counterstained with haematoxylin. Negative and positive controls for IHC included blocks of uninfected and SARS-CoV-2-infected Vero E6 cells, respectively.

For the quantification of N protein in the nasal turbinate epithelium, digitalized whole slide scans were analysed using the image analysis software HALO (Indica Labs). The respiratory epithelium was manually annotated to create a layer for downstream analysis. Area quantification was performed to determine the percentages of SARS-CoV-2 N in the annotated layer, which generated the percentage of immunoreactivity output.

Reporting summary

Further information on research design is available in the Nature Portfolio Reporting Summary linked to this article.

Data availability

All data supporting the conclusions of this study are reported in the paper. The raw data are available from the corresponding author with no restrictions upon reasonable request. Source data are provided with this paper.

Code availability

No code was used for data acquisition in this study.

55. Torii, S. et al. Establishment of a reverse genetics system for SARS-CoV-2 using circular polymerase extension reaction. Cell Rep. **35**, 109014 (2021).
56. Chen, D. Y. et al. SARS-CoV-2 disrupts proximal elements in the JAK-STAT Pathway. J. Virol. **95**, e0086221 (2021).
57. Tzou, P. L., Tao, K., Pond, S. L. K. & Shafer, R. W. Coronavirus Resistance Database (CoV-RDB): SARS-CoV-2 susceptibility to monoclonal antibodies, convalescent plasma, and plasma from vaccinated persons. PLoS ONE **17**, e0261045 (2022).
58. Rambaut, A. et al. A dynamic nomenclature proposal for SARS-CoV-2 lineages to assist genomic epidemiology. Nat. Microbiol. **5**, 1403–1407 (2020).
59. Aksamentov I, R. C., Hodcroft, E. & Neher, R. Nextclade: clade assignment, mutation calling and quality control for viral genomes. J. Open Source Softw. **6**, 3773 (2021).
60. Jacob, A. et al. Derivation of self-renewing lung alveolar epithelial type II cells from human pluripotent stem cells. Nat. Protoc. **14**, 3303–3332 (2019).

Author contributions M.S. conceptualized the study. D.-Y.C., C.V.C., D.K., A.H.T., S.A., N.K., H.L.C., F.D. and M.S. performed experiments. G.L. and M.U.G. established and provided the modified CPER system. N.A.C., H.P.G. and A.K.O. performed histopathological and IHC analysis of mouse lungs. R.N.K. generated the 3D image of the S protein. M.C.C. and J.Z.L. performed sequencing analyses of recombinant viruses. D.N.K. provided iPS-cell-derived alveolospheres. S.C.B. and M.B. provided scientific input. A.H. and A.E. provided BACs containing the SARS-CoV-2 genome. J.H.C. provided the Omicron isolate. Y.K. provided plasma samples. MS wrote the manuscript, which was read, edited and approved by all authors.

Article

Extended Data Fig. 1 | Schematic overview of mutations in Omicron S. Top, amino acid changes in Omicron S compared to the SARS-CoV-2 Wuhan-Hu-1 isolate (NCBI accession number: NC_045512). Numbering is based on Wuhan-Hu-1 sequence. Mutations not reported in previous variants of concern are shown in red. NTD, N-terminal domain; RBD, receptor-binding domain; RBM, receptor-binding motif. Bottom, location of Omicron changes on the trimeric S protein. Domains are coloured similarly in both panels.
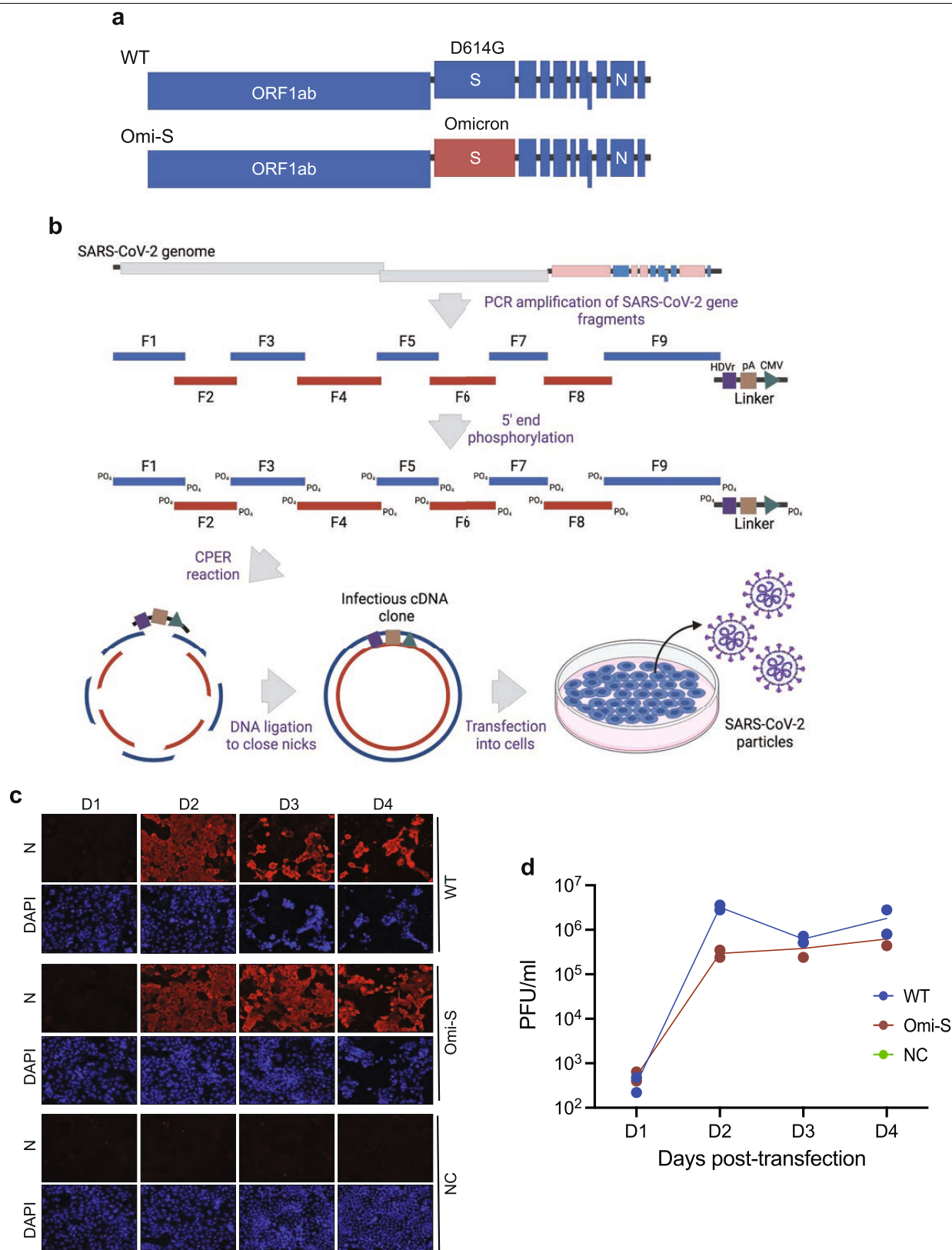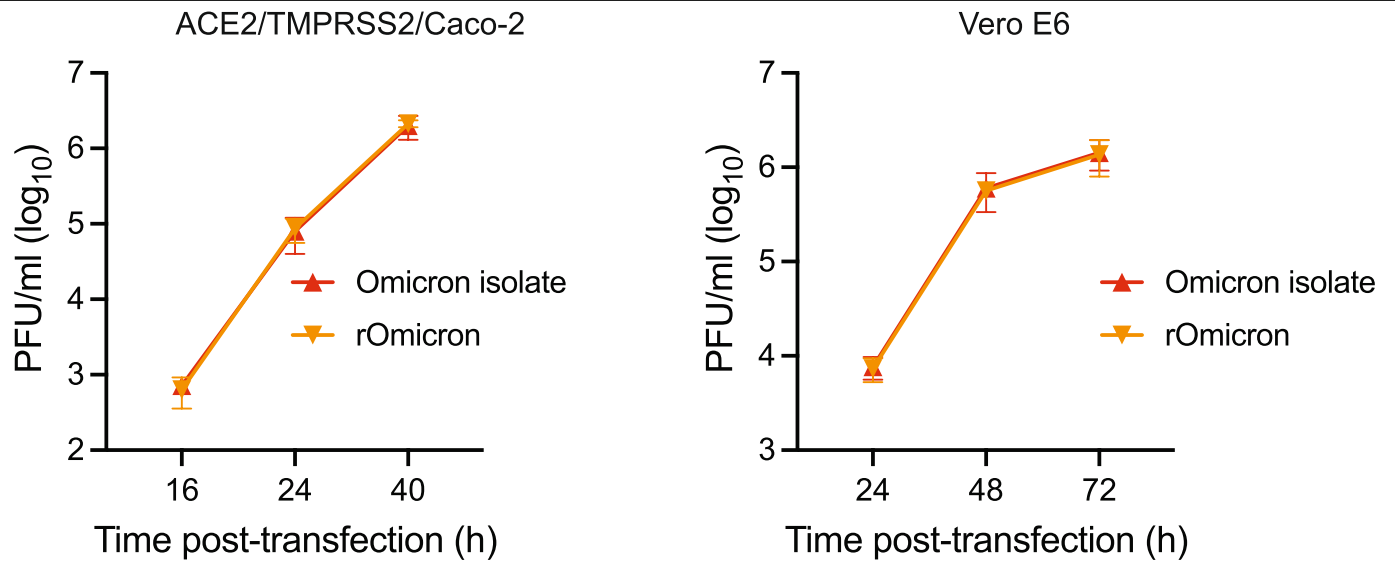
Extended Data Fig. 2 | Generating recombinant SARS-CoV-2 by CPER.
a, Schematic of recombinant SARS-CoV-2 generated by CPER (created with BioRender.com). S, spike; N, nucleocapsid. **b**, CPER protocol used in this study[24]. The SARS-CoV-2 genome was amplified into nine overlapping fragments. These fragments and a linker fragment (amplified from either pMW-CoV-2-UTRlinker or pGL-CPERlinker plasmid) were treated with PNK to phosphorylate 5′ ends. The 5′-end-phosphorylated fragments were then stitched together by CPER, and the nicks in the resulting circular DNA molecule were closed by treatment with DNA ligase. The CPER product was transfected into cells to rescue virus particles. **c**, ACE2/TMPRSS2/Caco-2 cells transfected with the SARS-CoV-2 CPER product were stained with an anti-nucleocapsid antibody on indicated days post-transfection. DAPI was used to stain the cell nuclei. NC, negative control generated by omitting fragment 9 from the CPER reaction. **d**, Virus titre in the culture medium of transfected cells at indicated days post-transfection, as measured by the plaque assay. The experiment was repeated twice. Individual values from both experiments are plotted.
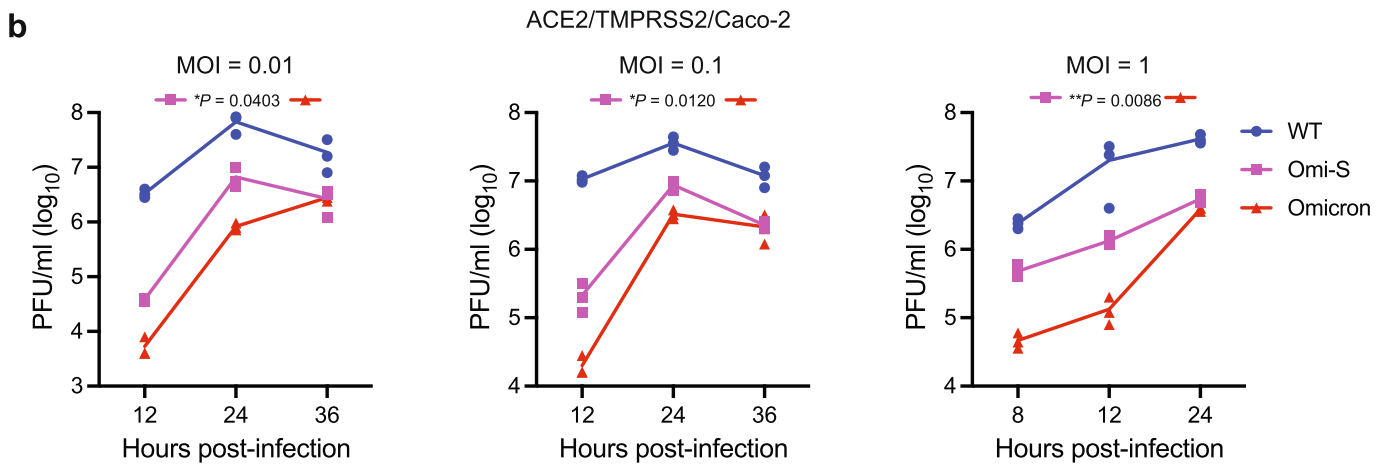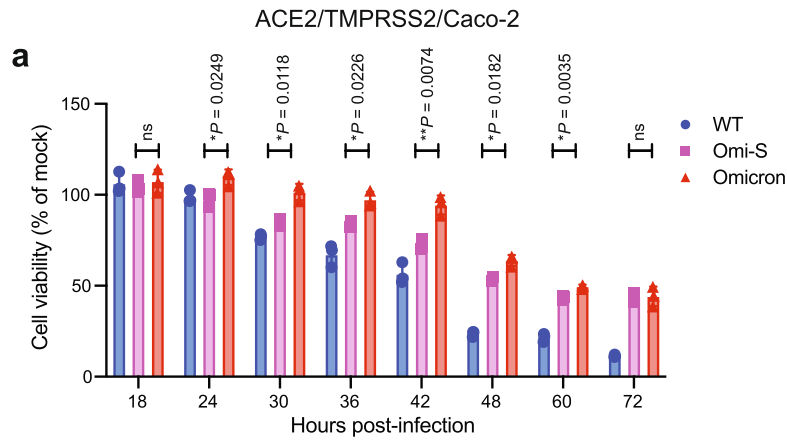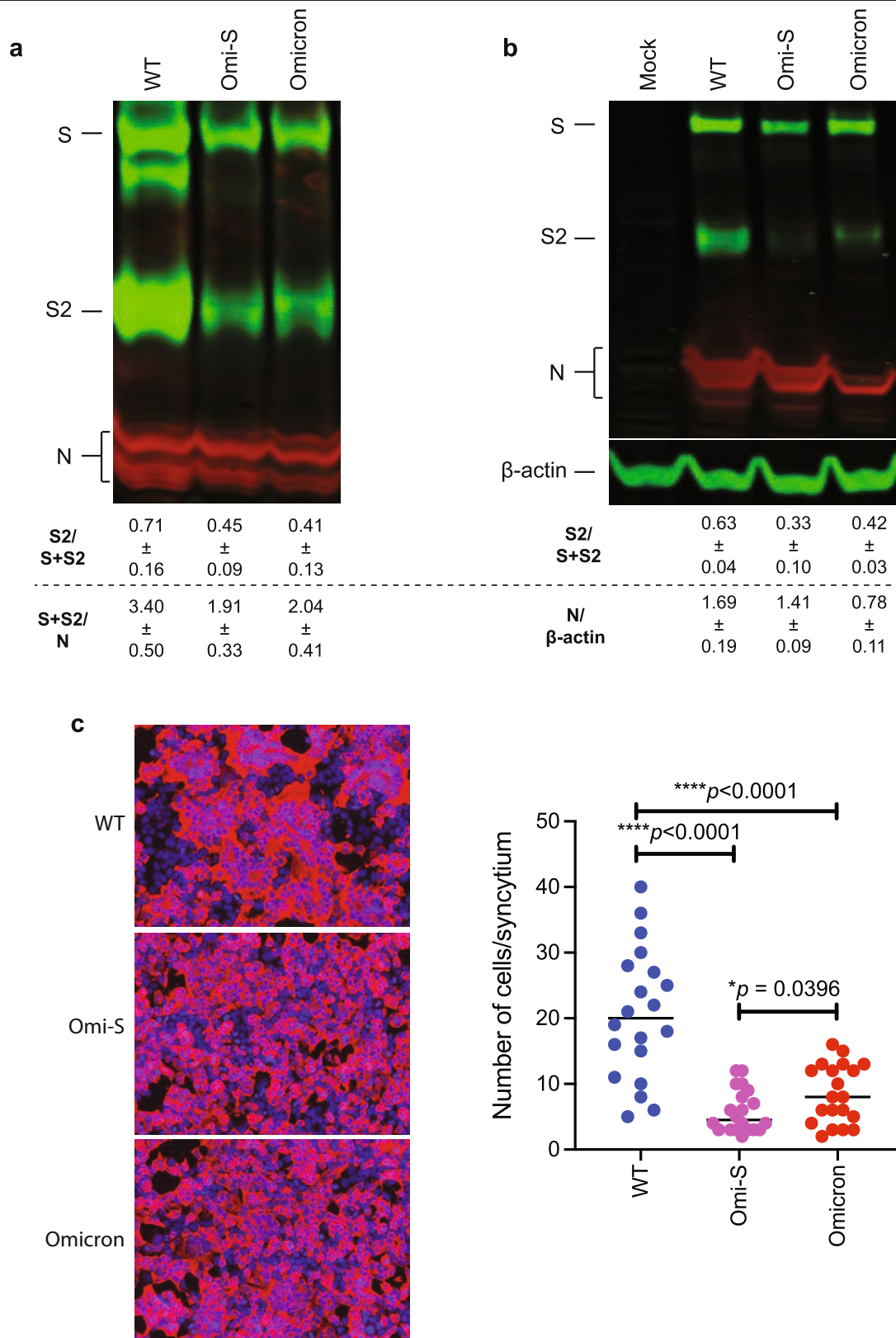
Extended Data Fig. 3 | Cytopathogenicity and replication of WT, Omi-S and Omicron in ACE2/TMPRSS2/Caco-2 cells. a, Cell viability of SARS-CoV-2-infected ACE2/TMPRSS2/Caco-2 cells (MOI of 0.1) was quantified by the CellTiter-Glo assay at indicated times of infection. *P* values indicate a statistically significant difference between Omi-S and Omicron (*n* = 3 replicates). **b**, ACE2/TMPRSS2/Caco-2 cells were infected with WT, Omi-S, and Omicron at an MOI of 0.01, 0.1, or 1, and the viral titre in the culture medium was measured by the plaque assay at indicated times post-infection. Statistically significant difference between Omi-S and Omicron has been shown for the middle time point (*n* = 3 replicates). *p* values were calculated by a two-tailed, unpaired *t*-test with Welch's correction. *P < 0.05, **P < 0.01, ***P < 0.001 and ****P < 0.0001; ns, not significant.

Extended Data Fig. 4 | Comparison of Omicron isolate and recombinant Omicron in cell culture. ACE2/TMPRSS2/Caco-2 (left) and Vero E6 (right) cells were infected with Omicron isolate or recombinant Omicron (generated by CPER) at an MOI of 0.01. The culture medium of infected cells was collected at indicated times, and the viral titre was measured by the plaque assay on ACE2/TMPRSS2/Caco-2 cells. The experiment was repeated twice, each time in three replicates. Error bars, mean ± s.d. (n = 3 replicates).

a

	WT	Omi-S	Omicron
S2/ S+S2	0.71 ± 0.16	0.45 ± 0.09	0.41 ± 0.13
S+S2/ N	3.40 ± 0.50	1.91 ± 0.33	2.04 ± 0.41

b

|	Mock	WT	Omi-S	Omicron
S2/ S+S2		0.63 ± 0.04	0.33 ± 0.10	0.42 ± 0.03
N/ β-actin		1.69 ± 0.19	1.41 ± 0.09	0.78 ± 0.11

c

Extended Data Fig. 5 | S-protein cleavage and fusogenicity of Omi-S and Omicron. a, Western blot of S incorporated into virus particles. Virions generated in ACE2/TMPRSS2/Caco-2 cells were concentrated, and equal amount of total protein was loaded in each lane. S (antibody against S2 domain) and N were detected. Numbers at the bottom indicate mean ± s.d. of two independent experiments. **b**, S in infected cell lysates. ACE2/TMPRSS2/Caco-2 cells, infected at an MOI of 0.01, were collected at 24 hpi and processed for western blot with antibodies against S2 and nucleocapsid. β-actin served as an internal control. Numbers at the bottom indicate mean ± s.d. of two independent experiments. For gel source data, see Supplementary Fig. 2. **c**, Immunofluorescence staining of ACE2/TMPRSS2/293T cells with anti-nucleocapsid antibody. Nuclei was stained with DAPI. Infection was carried out at an MOI of 1 for 18 h. Left, representative images; right, size of 20 syncytia from two experimental repeats. *P* values were calculated by a two-tailed, unpaired *t*-test with Welch's correction.
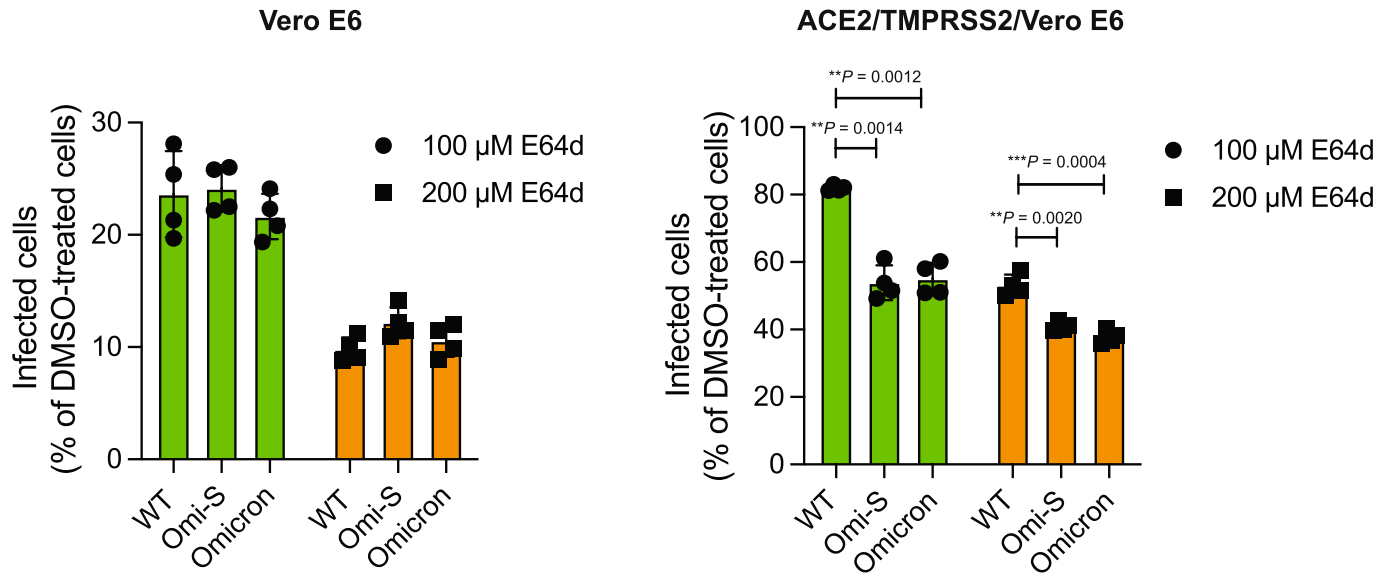
Extended Data Fig. 6 | Preferential cell entry of Omi-S and Omicron through the cathepsin-mediated pathway. Vero E6 or ACE2/TMPRSS2/Vero E6 cells treated with E64d for 2 h were infected at an MOI of 0.5 and stained with anti-nucleocapsid antibody at 24 hpi for immunofluorescence analysis. Bar graphs show the percentage of infected cells relative to a DMSO control, for which the values were arbitrarily set at 100. Error bars, mean ± s.d. ($n = 4$ replicates). The experiment was performed only once. P values were calculated by a two-tailed, unpaired t-test with Welch's correction.

a

b

Survived
Dead
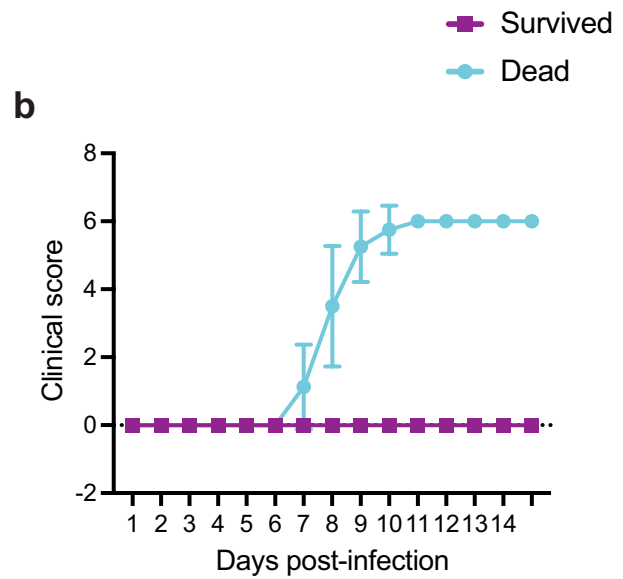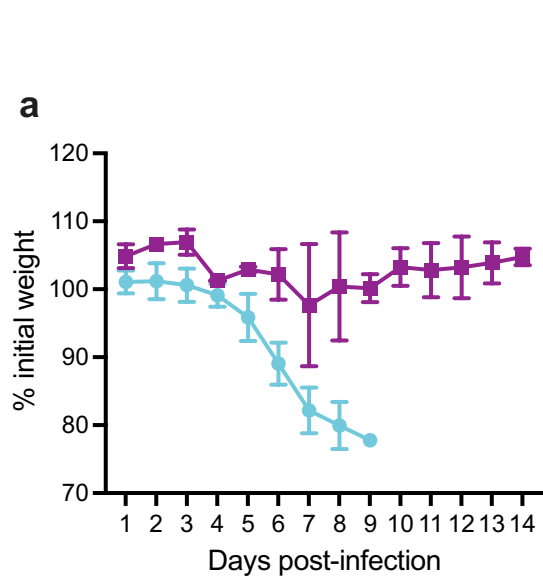
Extended Data Fig. 7 | Clinical signs in Omi-S-infected mice. a,b, K18-hACE2 mice (*n* = 10) inoculated intranasally with 1 × 10⁴ PFU of Omi-S and described in Fig. 2a–c were monitored for body weight (**a**) and clinical score (**b**). Mice that lost 20% of their body weight (8 out of 10) were euthanized. The surviving mice did not show any signs of distress.
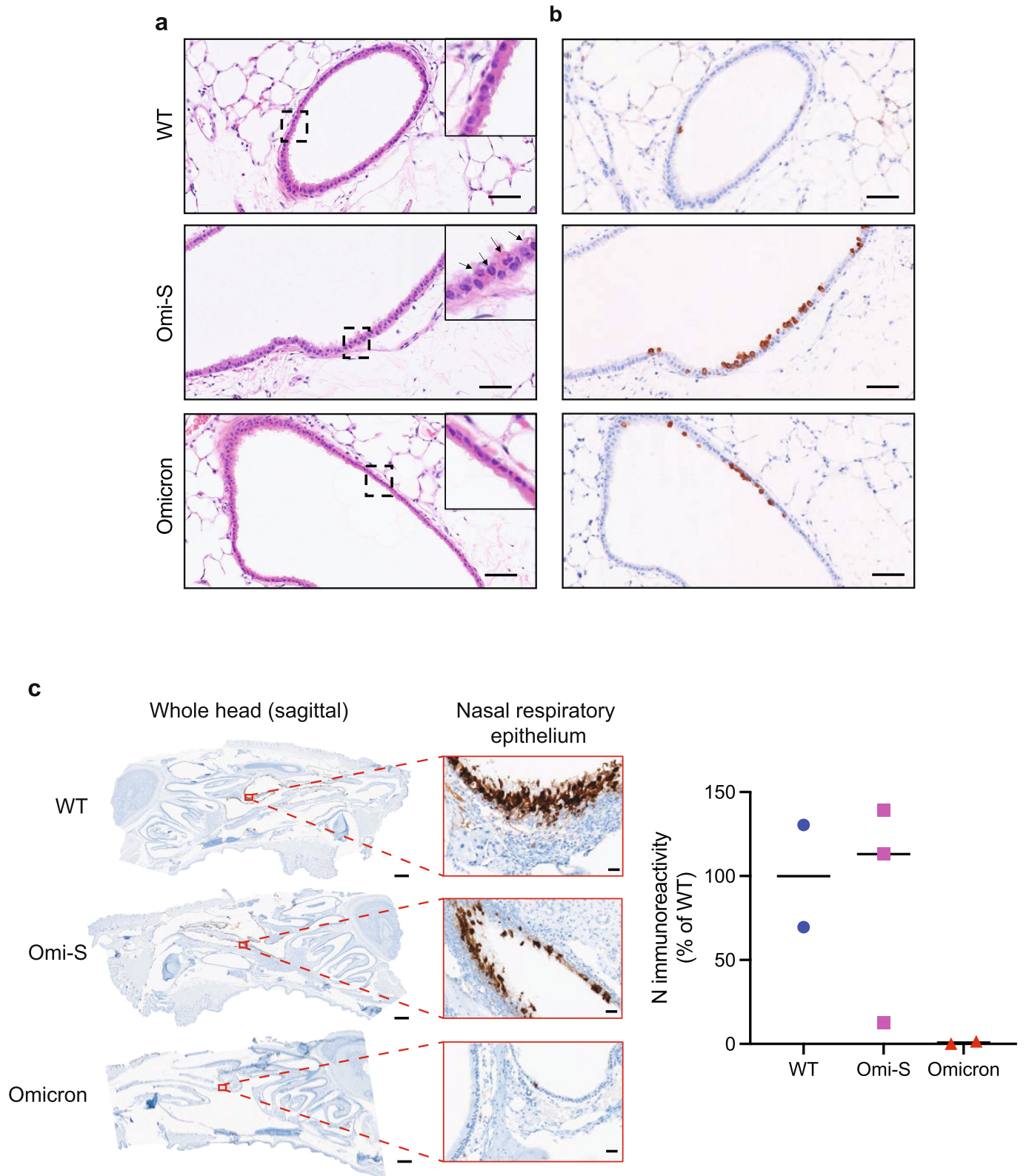
Extended Data Fig. 8 | Lung pathology and nasal turbinate IHC in mice infected with WT, Omi-S and Omicron. The lungs and nasal turbinates of K18-hACE2 mice intranasally inoculated with 1×10^4 PFU of WT, Omi-S and Omicron were collected at 2 dpi for histological analysis. **a**, Representative images of haematoxylin and eosin (H&E) staining for the detection of bronchiolar damage in the lungs of the infected mice. The bronchiolar epithelial necrosis is shown with arrows. **b**, IHC staining to detect SARS-CoV-2 S protein in the same area where bronchiolar necrosis was seen. No evidence of necrosis was found in bronchioles of mice infected with Omicron. Scale bars, 100 μm. **c**, Nucleocapsid distribution and abundance in the nasal passages of WT, Omi-S and Omicron. Left, representative images; Right, N immunoreactivity in nasal respiratory epithelium presented as percentage of the mean of WT (n = 2 mice for WT and Omicron; n = 3 mice for Omi-S). Chromogenic 3,3'-diaminobenzidine (DAB) IHC: (left panel, 12.5× total magnification; right panel, 400× total magnification). Higher-magnification views of nasal respiratory epithelium indicated by red squares are shown on the right. Scale bars: left, 800 μm; right, 20 μm.
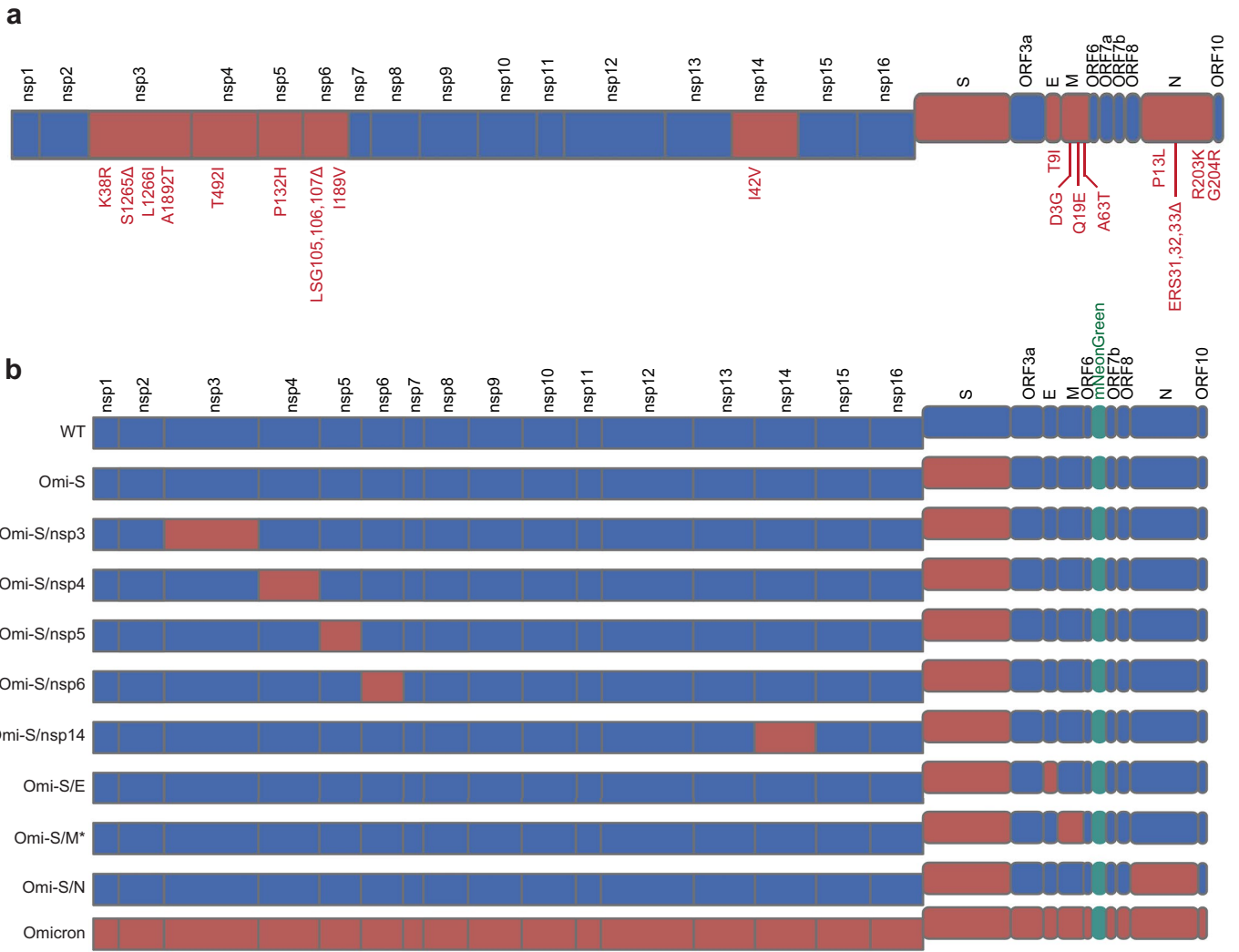
Extended Data Fig. 9 | Panel of chimeric viruses containing S and non-spike mutations. a, Amino acid changes outside of S in Omicron BA.1 compared to D614-containing ancestral SARS-CoV-2. Proteins with amino acid changes are shown in red, whereas wild-type proteins are in blue. Amino acid numbers are according to individual viral proteins. **b**, Schematic representation of recombinant viruses generated by CPER. ORF7a was being replaced with mNeonGreen to generate reporter viruses. *Sequencing analysis showed that Omi-S/M lacked the A63T mutation in M, despite it being present in the plasmid used for CPER. S, spike; E, envelope; M, membrane; N, nucleocapsid.
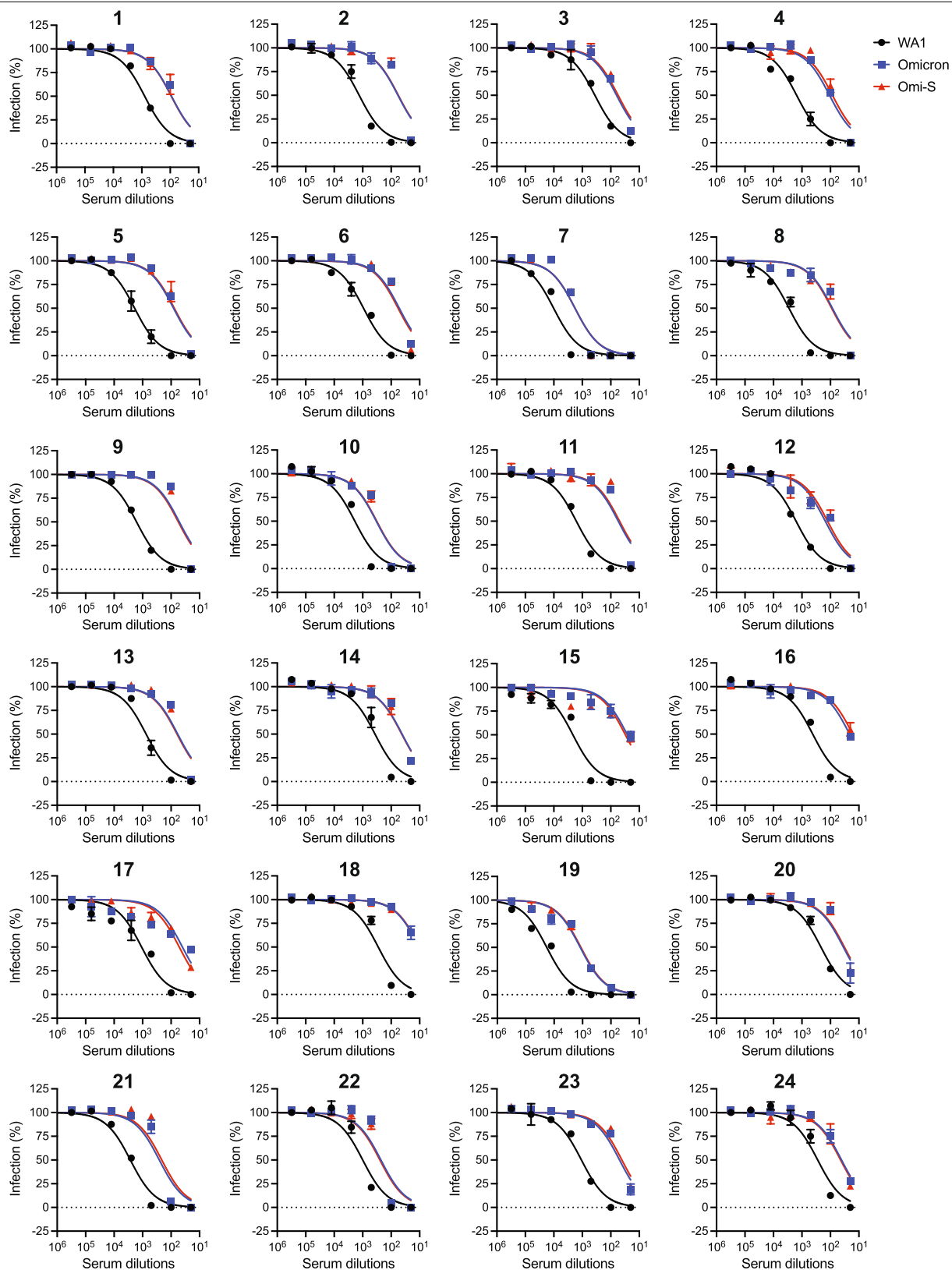
Extended Data Fig. 10 | Individual neutralization data. Individual neutralization curves for the data presented in Fig. 4a,b are shown. The data represent the mean ± s.d. of three technical replicates. The curves were calculated based on a non-linear regression curve fit analysis in Prism. The dotted lines represent the limit of detection.

Extended Data Table 1 | Information about serum samples

Serum no.	Sex	Race	Age	Days post-vaccination*	Vaccine (Manufacturer)	Spike Ab titer (AU/ml)**
1	Male	White	59	18	mRNA-1273 (Moderna)	39823.0
2	Male	Black	26	37	mRNA-1273 (Moderna)	26978.7
3	Male	Asian	55	34	mRNA-1273 (Moderna)	24880.7
4	Male	White	39	32	mRNA-1273 (Moderna)	23816.7
5	Male	Asian	45	38	mRNA-1273 (Moderna)	21659.5
6	Male	White	30	32	mRNA-1273 (Moderna)	18986.5
7	Female	Asian	47	35	mRNA-1273 (Moderna)	100000.0
8	Female	White	62	47	mRNA-1273 (Moderna)	69680.0
9	Female	White	39	14	mRNA-1273 (Moderna)	54996.6
10	Female	White	38	32	mRNA-1273 (Moderna)	46494.7
11	Female	White	34	30	mRNA-1273 (Moderna)	43784.0
12	Female	White	57	42	mRNA-1273 (Moderna)	42140.5
13	Male	Mixed	28	51	BNT162b2 (Pfizer-BioNTech)	17623.8
14	Male	White	30	54	BNT162b2 (Pfizer-BioNTech)	16154.5
15	Male	White	29	54	BNT162b2 (Pfizer-BioNTech)	14261.5
16	Male	Asian	48	48	BNT162b2 (Pfizer-BioNTech)	10593.6
17	Male	White	46	60	BNT162b2 (Pfizer-BioNTech)	9752.3
18	Male	White	31	53	BNT162b2 (Pfizer-BioNTech)	8715.2
19	Female	White	55	52	BNT162b2 (Pfizer-BioNTech)	100000.0
20	Female	White	43	47	BNT162b2 (Pfizer-BioNTech)	44385.4
21	Female	White	56	48	BNT162b2 (Pfizer-BioNTech)	39998.5
22	Female	Mixed	44	49	BNT162b2 (Pfizer-BioNTech)	31141.9
23	Female	White	56	50	BNT162b2 (Pfizer-BioNTech)	25969.6
24	Female	White	55	51	BNT162b2 (Pfizer-BioNTech)	23539.1

Overview of serum samples used for the analysis of antibody neutralization of WA1, Omi-S and Omicron. *Days after the second vaccine shot. **The spike antibody titre was measured by Abbott's SARS-CoV-2 immunoassays.

Corresponding author(s): Mohsan Saeed

Last updated by author(s): November 30, 2022

Reporting Summary

Nature Portfolio wishes to improve the reproducibility of the work that we publish. This form provides structure for consistency and transparency in reporting. For further information on Nature Portfolio policies, see our Editorial Policies and the Editorial Policy Checklist.

Statistics

For all statistical analyses, confirm that the following items are present in the figure legend, table legend, main text, or Methods section.

n/a	Confirmed	
☐	☒	The exact sample size (*n*) for each experimental group/condition, given as a discrete number and unit of measurement
☐	☒	A statement on whether measurements were taken from distinct samples or whether the same sample was measured repeatedly
☐	☒	The statistical test(s) used AND whether they are one- or two-sided *Only common tests should be described solely by name; describe more complex techniques in the Methods section.*
☒	☐	A description of all covariates tested
☒	☐	A description of any assumptions or corrections, such as tests of normality and adjustment for multiple comparisons
☐	☒	A full description of the statistical parameters including central tendency (e.g. means) or other basic estimates (e.g. regression coefficient) AND variation (e.g. standard deviation) or associated estimates of uncertainty (e.g. confidence intervals)
☐	☒	For null hypothesis testing, the test statistic (e.g. *F*, *t*, *r*) with confidence intervals, effect sizes, degrees of freedom and *P* value noted *Give P values as exact values whenever suitable.*
☒	☐	For Bayesian analysis, information on the choice of priors and Markov chain Monte Carlo settings
☒	☐	For hierarchical and complex designs, identification of the appropriate level for tests and full reporting of outcomes
☒	☐	Estimates of effect sizes (e.g. Cohen's *d*, Pearson's *r*), indicating how they were calculated

Our web collection on statistics for biologists contains articles on many of the points above.

Software and code

Policy information about availability of computer code

Data collection	No software was used for data collection
Data analysis	GraphPad Prism Version 9.4.1 was used to perform statistical analyses. FlowJo Version was used to analyze the flow cytometry data.

For manuscripts utilizing custom algorithms or software that are central to the research but not yet described in published literature, software must be made available to editors and reviewers. We strongly encourage code deposition in a community repository (e.g. GitHub). See the Nature Portfolio guidelines for submitting code & software for further information.

Data

Policy information about availability of data

All manuscripts must include a data availability statement. This statement should provide the following information, where applicable:

- Accession codes, unique identifiers, or web links for publicly available datasets
- A description of any restrictions on data availability
- For clinical datasets or third party data, please ensure that the statement adheres to our policy

All data supporting the conclusions of this study are reported in the paper. The raw data are available from the corresponding author with no restrictions upon reasonable request.

Human research participants

Policy information about studies involving human research participants and Sex and Gender in Research.

Reporting on sex and gender	N/A
Population characteristics	N/A
Recruitment	N/A
Ethics oversight	N/A

Note that full information on the approval of the study protocol must also be provided in the manuscript.

Field-specific reporting

Please select the one below that is the best fit for your research. If you are not sure, read the appropriate sections before making your selection.

☒ Life sciences ☐ Behavioural & social sciences ☐ Ecological, evolutionary & environmental sciences

For a reference copy of the document with all sections, see nature.com/documents/nr-reporting-summary-flat.pdf

Life sciences study design

All studies must disclose on these points even when the disclosure is negative.

Sample size	In vitro studies: No sample-size calculation was performed a priori. All experiments with statistical analyses were repeated at least twice, each with multiple technical replicates. In vivo studies: Cohort sizes were determined based on our previous SARS-CoV-2 studies in animals (PMID: 35336942) and others' animal studies (PMID: 35062015). We used n=7-10 for death/survival studies, n=4 for monitoring viral load in the lung of infected animals, and n= 2 or 3 for IHC.
Data exclusions	No data were excluded from the analyses.
Replication	Each experiment was repeated at least twice and the results were successfully reproduced. To confirm the authenticity of our results, we repeated our experiments with independently generated virus stocks.
Randomization	There are no experimental groups in our study, so this does not apply.
Blinding	There are no group allocations in this study, so this does not apply.

Reporting for specific materials, systems and methods

We require information from authors about some types of materials, experimental systems and methods used in many studies. Here, indicate whether each material, system or method listed is relevant to your study. If you are not sure if a list item applies to your research, read the appropriate section before selecting a response.

Materials & experimental systems

n/a	Involved in the study
☐	☒ Antibodies
☐	☒ Eukaryotic cell lines
☒	☐ Palaeontology and archaeology
☐	☒ Animals and other organisms
☐	☐ Clinical data
☒	☐ Dual use research of concern

Methods

n/a	Involved in the study
☒	☐ ChIP-seq
☐	☒ Flow cytometry
☒	☐ MRI-based neuroimaging

Antibodies

Antibodies used	For flow cytometry: Rabbit anti-SARS-CoV nucleocapsid polyclonal antibody (Rockland; #200-401-A50; 1:1000) Donkey anti-Rabbit IgG-AF647 secondary antibody (ThermoFisher Scientific; #A-31573; 1:1000)

Validation	For IF: Rabbit anti-SARS-CoV nucleocapsid polyclonal antibody (Rockland; #200-401-A50; 1:2000) Alexa Fluor 568-conjugated goat anti-Rabbit secondary antibody (Invitrogen; #A11008; 1:1000) For IHC: Mouse anti-SARS-CoV nuceocapsid monoclonal antibody (Cell Signaling Technologies; #68344; 1:1000) (For the SARS-CoV-2 N antibody, given its mouse origin, an additional rabbit anti-mouse anti-Ig1 + Ig2a + IgG3 antibody (Abcam; #133469; 1:1000) was used to prevent non-specific binding.) Anti-SARS-CoV-2 spike protein (S1) antibody (Cell Signaling Technology; # 99423; 1:400) For Western Blot: Rabbit anti-SARS-CoV nucleocapsid polyclonal antibody (Rockland; #200-401-A50; 1:1000) Mouse anti-SARS-CoV-2 spike monoclonal antibody (GeneTex; #GTX632604; 1:1000) IRDye 800CW Donkey anti-Mouse IgG secondary antibody (LI-COR Biosciences; #926-32212; 1:5000) IRDye 680RD Donkey anti-Rabbit IgG secondary antibody (LI-COR Biosciences; #926-68073; 1:5000)
	Rabbit anti-SARS-CoV nucleocapsid polyclonal antibody (Rockland; #200-401-A50; 1:1000) Mouse anti-SARS-CoV nuceocapsid monoclonal antibody (Cell Signaling Technologies; #68344; 1:1000) Anti-SARS-CoV-2 spike protein (S1) antibody (Cell Signaling Technology; # 99423; 1:400) Rabbit anti-SARS-CoV nucleocapsid polyclonal antibody (Rockland; #200-401-A50; 1:1000) Mouse anti-SARS-CoV-2 spike monoclonal antibody (GeneTex; #GTX632604; 1:1000) These antibodies were validated using uninfected cells as negative controls. No signal was obtained in uninfected cells. Donkey anti-Rabbit IgG-AF647 secondary antibody (ThermoFisher Scientific; #A-31573; 1:1000) Alexa Fluor 568-conjugated goat anti-Rabbit secondary antibody (Invitrogen; #A11008; 1:1000) IRDye 800CW Donkey anti-Mouse IgG secondary antibody (LI-COR Biosciences; #926-32212; 1:5000) IRDye 680RD Donkey anti-Rabbit IgG secondary antibody (LI-COR Biosciences; #926-68073; 1:5000) These are secondary antibodies extensively validated by the providers for flow cytometry, IF, and western blot. As described in the Method section, these antibodies worked optimally with our protocols.

Eukaryotic cell lines

Policy information about cell lines and Sex and Gender in Research

Cell line source(s)	Human embryonic kidney HEK293T cells (ATCC; CRL-3216), human lung adenocarcinoma A549 cells (ATCC; CCL-185), African green monkey kidney Vero E6 cells, and human colorectal adenocarcinoma Caco-2 cells (ATCC; HTB-37), and human induced pluripotent stem cell-derived alveolar type 2 epithelial cells.
Authentication	None of the cell lines was authenticated.
Mycoplasma contamination	All cell types described were regularly tested and found to be mycoplasma-free.
Commonly misidentified lines (See ICLAC register)	No commonly misidentified cell lines were used in this study.

Animals and other research organisms

Policy information about studies involving animals; ARRIVE guidelines recommended for reporting animal research, and Sex and Gender in Research

Laboratory animals	Heterozygous K18-hACE2 C57BL/6J mice (Strain 2B6.Cg-Tg(K18-ACE2)2Prlmn/J) were purchased from the Jackson Laboratory (Jax, Bar Harbor, ME). Both male and female mice in the age range of 12-20 weeks were being used. Mice were housed in groups of 4 to 5 and maintained on a 12:12 light cycle at 30-70% humidity and 68F temperature. The mice were provided water and standard chow diet (LabDiet, St. Louis, MO, USA) ad libitum.
Wild animals	No wild animals were used in this study.
Reporting on sex	Both male and female mice in the age range of 12-20 weeks were being used.
Field-collected samples	No field collected samples were used.
Ethics oversight	Animal studies were performed following the recommendations in the Guide for the Care and Use of Laboratory Animals of the National Institutes of Health. The protocols were approved by the Boston University Institutional Animal Care and Use Committee (IACUC).

Note that full information on the approval of the study protocol must also be provided in the manuscript.

Clinical data

Clinical trial registration	*Provide the trial registration number from ClinicalTrials.gov or an equivalent agency.*
Study protocol	*Note where the full trial protocol can be accessed OR if not available, explain why.*
Data collection	*Describe the settings and locales of data collection, noting the time periods of recruitment and data collection.*
Outcomes	*Describe how you pre-defined primary and secondary outcome measures and how you assessed these measures.*

Flow Cytometry

Plots

Confirm that:

☒ The axis labels state the marker and fluorochrome used (e.g. CD4-FITC).

☒ The axis scales are clearly visible. Include numbers along axes only for bottom left plot of group (a 'group' is an analysis of identical markers).

☒ All plots are contour plots with outliers or pseudocolor plots.

☒ A numerical value for number of cells or percentage (with statistics) is provided.

Methodology

Sample preparation	For flow cytometry, fixed cells were permeabilized in 1x permeabilization buffer (ThermoFisher Scientific; #00-5523-00) and stained with SARS-CoV-2 nucleocapsid antibody (Rockland; #200-401-A50), followed by donkey anti-rabbit IgG-AF647 secondary antibody (ThermoFisher Scientific; #A-31573). Gating was based on uninfected stained control cells. The extent of staining was quantified using a BD LSR II flow cytometer (BD Biosciences, CA), and the data were analyzed with FlowJo v10.6.2 (FlowJo, Tree Star Inc). For some experiments, we used fluorescently labeled viruses. In these cases, fixed cells were permeabilized in 1x permeabilization buffer (ThermoFisher Scientific; #00-5523-00) and subjected to flow cytometry. Gating was based on uninfected stained control cells. Where needed, single-color cells were used as controls. The extent of staining was quantified using a BD LSR II flow cytometer (BD Biosciences, CA), and the data were analyzed with FlowJo v10.6.2 (FlowJo, Tree Star Inc).
Instrument	LSR-II
Software	FlowJo
Cell population abundance	Since we worked only with the cell lines, we did not determine the purity of cells.
Gating strategy	The FSC/SSC gates were applied, before the cells were separated into SARS-CoV-2 positive and negative cell populations. When dealing with cells infected with two distinctly-colored viruses, we used single-color cells as controls.

☒ Tick this box to confirm that a figure exemplifying the gating strategy is provided in the Supplementary Information.